Assessing Dual-Polarization Radar Estimates of Extreme Rainfall During Hurricane Harvey

David B. Wolff*
NASA Goddard Space Flight Center, Wallops Flight Facility, Wallops Island, Virginia

Walter A. Petersen
NASA Marshall Space Flight Center, Huntsville, Alabama

Ali Tokay
Joint Center for Earth Systems Technology, University of Maryland Baltimore County
NASA Goddard Space Flight Center, Greenbelt, Maryland

David A. Marks
Science Systems & Applications, Inc., Lanham, Maryland
NASA Goddard Space Flight Center, Wallops Flight Facility, Wallops Island, Virginia

&

Jason L. Pippitt
Science Systems & Applications, Inc., Lanham, Maryland
NASA Goddard Space Flight Center, Greenbelt, Maryland

Submitted to Journal of Atmospheric and Oceanic Technology

First submission; May 6, 2019

Resubmitted: September 13, 2019

* Corresponding Author's Address:
NASA Wallops Flight Facility, Code 610.W
Wallops Island, VA 23337
757-824-1515
David.B.Wolff@nasa.gov

Abstract

Hurricane Harvey hit the Texas Gulf Coast as a major hurricane on August 25, 2017 before exiting the state as a tropical storm on August 29, 2017. Left in its wake was historic flooding, with some locations measuring more than 60 inches of rain over a five-day period. The WSR-88D radar (KHGX) maintained operations for the entirety of the event. Rain gauge data from the Harris County Flood Warning System (HCFWS) was used for validation with the full radar data set to retrieve daily and event-total precipitation estimates for the period August 25-29, 2017. The KHGX precipitation estimates were then compared to the HCFWS gauges. Three different hybrid polarimetric rainfall retrievals were used, along with attenuation-based retrieval that employs the radar-observed differential propagation. An advantage of using a attenuation-based retrieval is its immunity to partial beam blockage and calibration errors in reflectivity and differential reflectivity. All of the retrievals are susceptible to changes in the observed Drop Size Distribution (DSD). No *in situ* DSD data were available over the study area, so changes in the DSD were interpreted by examining the observed radar data. We examined the parameter space of two key values in the attenuation retrieval to test the sensitivity of the rain retrieval. Selecting a value of α=0.015 and β=0.600 and β=0.625 provided the best overall results, relative to the gauges, but more work needs to be done to develop an automated technique to account for changes in the ambient DSD.

1. Introduction

The hazards of hurricanes include strong winds, associated tornadoes, heavy rains, and storm surge. However, according to Blake and Zelinsky (2018) and others, about 90% of hurricane-related fatalities are caused by coastal and inland floodwaters, and Hurricane Harvey (2017) was no exception. At least 103 people died in Harvey-related incidents, 68 of them from direct impacts including flooding throughout Texas. Blake and Zelinsky (2018) also reported that more than 17,000 people had been rescued and an estimated 30,000 were displaced across the state. Hurricane Harvey tied with Hurricane Katrina (2005) as the costliest tropical cyclone on record, inflicting $125 billion in damage, primarily from catastrophic rainfall-triggered flooding in the Houston metropolitan area.

Harvey started as a weak tropical storm near the Lesser Antilles on August 17, 2017 and then dissipated over the central Caribbean Sea (Blake and Zelinsky, 2018). However, after crossing the Yucatan peninsula on August 24, 2017, it reformed over the Bay of Campeche and rapidly developed into a Category 4 hurricane before making landfall on the middle Texas coast on August, 25, 2017 at 0300 UTC. The eye made landfall on the northern end of San Jose Island, near Rockport, TX with maximum sustained winds of 115 kt (59 m s^{-1}) and minimum central pressure of 937 mb. The storm then made a second landfall three hours later on the Texas mainland (on the northeast coast of Copano Bay) with maximum sustained winds of 105 kt (54 m s^{-1}) and minimum central pressure of 948 mb. By 0600 UTC on August 25, 2017, Harvey had weakened over land to a tropical storm and maintained a 35 kt (18 m s^{-1}) intensity for the next two days. The storm then stalled southeast of San Antonio, TX for several days dropping copious amounts of rain over southeast Texas before finally reemerging over the Gulf of Mexico on August 28, 2017. The storm then made a third and final landfall near Cameron, LA, on August 29, 2017 and headed rapidly northeastward across Louisiana, Mississippi, Tennessee and Kentucky. Figure 1 provides the track of Harvey using the National Hurricane Center (https://www.nhc.noaa.gov) best track data (HURDAT2). Given such extreme rainfall over this period, it is important to determine how well conventional, and unconventional rain estimates perform.

The National Weather Service (NWS) dual-polarimetric radar (KHGX), located southeast of Houston, maintained operations for the entirety of the event. The Harris County Flood Warning System (HCFWS) had over 200 rain gauges deployed in its network concentrated in a relatively compact area of roughly 200 km^2. Figure 2 is a map of southeast Texas with the KHGX radar in the middle. Range rings of 25, 50 and 75 km are provided. The rectangle to the northwest represents the area over which many of the radar statistics are calculated throughout the paper. The selected gauge locations are shown as blue triangles. The polygon within the rectangle is a rough outline of Harris County.

With the advent of dual-polarimetric radars by the National Weather Service, the ability to accurately retrieve rain rates in a variety of precipitation types is now possible (Ryzhkov and Zrnić 1995; Brandes et al. 2002; Bringi et al. 2004, 2011; Giangrande and Ryzhkov 2008; Wang et al. 2013, 2019; Chen et al. 2017; Cocks et al. 2019).

In order to properly quantify rainfall, a dense rain gauge network and dual-polarization weather radar are currently the best resources available. During Harvey, both data sources were available. Unfortunately, no disdrometer data that could be used to validate the evolving drop size distribution (DSD) was available. In this study, we used the full radar data set to retrieve daily and event-total precipitation estimates within 75 km of the KHGX radar for the period August 25-29, 2017. These estimates were then compared to the selected HCFWS gauges. Four different rain retrievals were used: three polarimetric "hybrid" rainfall algorithms, which utilize observed values of horizontal reflectivity Z_H, differential reflectivity Z_{DR} and differential phase Φ_{DP}, from which the specific differential phase K_{DP} is calculated, and an attenuation-based retrieval that uses observed values of Z_H and differential propagation phase Φ_{DP}. The hybrid estimators and associated methodologies used were: Cifelli et al. 2011, hereafter RC; Bringi et al. 2004, hereafter RP; and Chen et al. 2017, hereafter RR. We note that these hybrid estimators are currently used by NASA's Global Precipitation Measurement (GPM) (Hou et al. 2014) Ground Validation (GV) team for routine validation of GPM satellite estimates. The radar observed differential phase Φ_{DP} was also used to employ an attenuation-based retrieval, hereafter RA, following Ryzhkov et al. 2014. One advantage of using the RA approach is that the phase measurement it relies on is relatively immune to blockage and calibration errors of both the reflectivity and differential reflectivity.

In the remainder of this paper Section 2 will discuss the data used in this study and described the quality control procedures utilized. Section 2 will also provide details of the rain rate retrievals used. Section 3 will present comparisons between the several radar retrievals and rain gauges. Section 4 will discuss how the sensitivity of the RA retrievals to changes α *and* β. Section 5 will discuss changes in DSD over the Harvey event and how they relate to changes in the radar retrievals. Finally, Section 6 will provide our summary and conclusions.

2. Data

a. Gauge Data

The gauge data used for this study was obtained on-line from the Harris County Flood Warning System. According to the HCFWS web site, data-collecting sensors at each tipping bucket gauge station transmit rainfall amounts via radio frequency after 0.04 inches of rain is measured by a sensor. Shortly after the Harvey event, we downloaded data from 244 gauges; however, more than half of those that were outside of the box shown in Fig. 2 were removed. We further eliminated another 21 gauges because they were located along radar azimuths with known radar beam blockages. The dashed lines show the blocked area (298° - 306°). According to Mark Moore (*personal communication*), a Hydrologic Specialist with the Harris County Flood Control District (HCFCD), all of the rain gauges are checked to assure that they meet the specifications of the manufacturer every 6 months. For the tipping buckets they use, this represents an accuracy of ± 3% at rainfall rates up to 2 inches per hour. Any tipping buckets that do not meet this standard are rejected. Given the inherent uncertainty of these types of gauges due to rainfall rate errors and other environmental factors, HCFCD estimates a total uncertainty of approximately ±10-15%.

b. Radar Data

The radar data used in this study was obtained from the KGHX WSR-88D radar located in League City, TX, which is southeast of Houston. Fortunately, the radar operated continuously throughout the five-day event. Based on frequent use of this radar data and comparisons to space-borne reflectivities (Schwaller and Morrison, 2011) from NASA's Global Precipitation Measurement (GPM) mission (Hou et al. 2014) both the radar reflectivity and differential reflectivity were both well calibrated. The data consisted of full volume scans taken roughly every 5-6 minutes. We note that the specific differential phase used in this study was obtained from the DROPS2.0 algorithm (Chen et al. 2017).

To provide quality control (QC) of the KHGX data, we employed the same dual-polarimetric quality control (DPQC) procedures applied to radar data as those routinely generated by the Global Precipitation Measurement (GPM) mission Ground Validation (GV) Program (Ryzhkov and Zrnic 1998b; Zrnic and Ryzhkov 1999; Cifelli et al. 2002). Specifically, GPM GV adapted a series of algorithms based on Ryzhkov et al. 1998 for conducting DPQC. The DPQC algorithms are successful in identifying and removing non-precipitating echoes (Ryzhkov and Zrnic 1998; Zrnic and Ryzhkov 1999; Ryzhkov et al. 2005; Cifelli et al. 2002) and unfolding of Φ_{DP}.

c. Radar data quality control

The DPQC algorithm initially uses its default thresholds which produces a mostly clean radar product. The default data were then reviewed and additional manual adjustments were made to produce the highest quality radar product. These manual adjustments are subjective tweaks that are applied by GPM GV radar specialists. See Marks et al. 2011 for a more detailed description of the DPQC method. The DPQC threshold modules are dependent on the observed values associated with many of the observed radar fields. When the value of a gate fell outside one of the thresholds, a missing data mask was applied to that specific gate for all fields. Each threshold module has utility for removing non-precipitating echoes. Primary fields for QC threshold modules include measured reflectivity DZ, differential reflectivity DR, cross-polar correlation RH, signal quality index SQ, differential phase PH, and specific differential phase KD. The output or “corrected” reflectivity field is given by CZ. Once the CZ map has been generated, the pixels with no-precipitation echo are used to mask all the other fields. A flow chart of the DPQC algorithm is presented in Fig. 3.

d. Radar rain retrievals

Once the data was properly QC'd, several additional routines were executed to calculate K_{DP} (Chen et al. 2017), hybrid DP rain estimates (RC, RP and RR), DSD retrievals of mass-weighted mean diameter DM and normalized slope parameter NW (Tokay et al. 2019), and the attenuation-based rain estimate RA based on Ryzhkov et al. 2014. The QC'd radar data was gridded using NCAR's RadX software. The horizontal and vertical resolution of the gridded data was 1 km, extending 100 km horizontally and 15 km vertically from the KHGX radar. From here onward, the following abbreviations will be made for the quality-controlled and calibrated field: reflectivity CZ; differential reflectivity DR; and specific differential phase KD.

As previously mentioned, we generated three hybrid dual-polarization rain estimates following RC, RP and RR. We refer these as hybrid estimates because, unlike conventional Z-R relationships that rely solely on CZ, these estimates consider different values of CZ, DR and KD to determine the associated rain rate. We refer the reader to these references for a full description of these retrievals, but provide a general overview here.

While the RC method was originally developed for application to Colorado precipitation, the GPM GV team has found it to be an excellent approach in other regions as well (e.g. Delmarva Peninsula, Melbourne, FL; Kwajalein, RMI). A flowchart of the RC method is provided in Fig. 4. The full implementation of the RC algorithm makes a distinction between rain and ice (Seo et al. 2018); however, given the tropical nature of this event, we limit the analysis in this study to rain only.

The RP method uses the respective values of CZ, DR and KD to first retrieve DSD parameters D_0, N_W and μ, which are the median drop diameter, normalized intercept parameter and shape function, respectively. These parameters are retrieved by examining the values of CZ, DR, and KD by assuming that a gamma distribution (Atlas and Ulbrich, 1977) properly describes the DSD. The algorithm then derives a dynamically changing coefficient to a standard Z-R equation. The default Z-R equation proposed by Bringi et al. 2004 is given by $Z=a * R^{b}$., where *a* and *b* are 219 and 1.45, R is in mm hr^{-1}, and Z is in mm^6 m^{-3}respectively. Based on the values of the CZ, DR, and KD, the coefficient *a* is replaced with *a'* on a pixel-by-pixel basis. We follow the same logic as B04 but chose our default *a* and *b* values to be 300 and 1.4, respectively. A flowchart of the PolZR algorithm is provided in Fig. 5.

The third hybrid approached is referred to as DROPS2.0 and is fully discussed in Chen et al. 2017. DROPS2.0 is quite similar to DROPS1.0, which was derived from RC, but has been improved via better quality control and K_{DP} estimation, region-based hydrometeor classification, and rainfall estimation. It should be noted that the K_{DP} derived from the KHGX data used in this study was obtained from the DROPS2.0 program output.

Following Ryzhkov et al. 2014 (R14), we also constructed an attenuation-based rain rate retrieval. A flowchart showing our implementation of the RA method is given in Fig. 6. It is important to note that we made several modifications to the R14 approach. These changes were necessary to assure that we used data only of the highest quality. For clarity, we provide the equations discussed by R14 and intermediate steps taken to deal with quality-control issues of the differential phase data Φ_{DP}. The first step was to set the default rain rate as that provided by the RC estimator. Then for each ray in each sweep, all "speckle" or isolated pixels were removed. To prevent noisy edge effects, the beginning and ending of each segment was averaged over three 250 m range gates. Once this was completed, the $\Delta\Phi_{DP}$ across each rain segment in a ray was calculated. If $\Delta\Phi_{DP} > 3$ degrees along the entire ray, then the ray was processed. If not, the RC rain rates for that ray were used.

If the $\Delta\Phi_{DP}$ threshold was satisfied then the following was performed. Using Path Integrated Attenuation (PIA; Meneghini and Nakamura 1990; Iguchi and Meneghini 1994, Testud et al. 2000, Bringi et al. 1990) as defined in Eq. 2 below

$$PIA = \alpha * \Delta\Phi_{DP} \qquad (2),$$

where PIA is the path integrated attenuation along the ray, and the factor α is the net ratio of A and K_{DP} along the path, and is a function of the DSD (Wang et al. 2019).

$$I(r_1, r_2) = 0.46 * \beta * \Sigma(Z)^{\beta} \qquad (3),$$

In Eq. 3, $I(r_1, r_2)$ is the integrated reflectivity along the each rain segment in a ray using the linear reflectivity Z [$mm^6\ m^{-3}$], where β is a constant between 0.6 – 0.9 at microwave frequencies (R14), and r_1 and r_2 are the first and last valid gates of the each rain segment, respectively.

Then for each gate along the ray with a valid Φ_{DP} value, the reflectivity was integrated from the given gate to the last valid gate, given by

$$I(r, r_2) = 0.46 * \beta * \Sigma(Z)^{\beta} \qquad (4),$$

where $I(r, r_2)$ is the integrated reflectivity from the current gate r to the last valid gate r_2. According to R14, the RA method is only valid in non-frozen precipitation, so the height of each gate was checked and compared to the current sounding to assure that the current radar gate was below the freezing level. If the temperature T at the height of a given gate was > 0C, then the following parameters are calculated:

$$C_1 = (2.23 + 0.078*T + 0.00085*T^2) * 10^3 \quad (5)$$

$$C_2 = 1 - 0.25(11 - \lambda) \quad (6)$$

where T is the ambient temperature at the height of the given radar gate, and l is the radar wavelength. Tthe total attenuation was given by

$$A = (C * (Z^\beta))/ (I(r_1, r_2) + C * I(r, r_2)) \quad (7)$$

Finally, the rain rate at a given gate was then given by a power law of the attenuation:

$$RA = C_1 * C_2 * A^{1.03} \quad (8)$$

According to R14, their approach is relatively immune to radar reflectivity Z biases and differential reflectivity calibration, as well as wet radome effects, partial beam blockage, and inadequate correction for attenuation. Also, rain-rate fields estimated from RA have the same spatial resolution and structure as R(Z), whereas the shapes of rain cells retrieved by R(K_{DP}) can be slightly distorted and the fields of R(K_{DP}) are much noisier, particularly at lower rain rates.

There are two critical parameters utilized in the RA method. The first, α is the defined as the net ratio of attenuation A and K_{DP} along the path, and is sensitive to the DSD, temperature and radar wavelength (R14; Wang et al. 2019). Hence, it requires optimization for a particular rain regime. R14 suggested a value of α=0.015 at S-band (Wang et al. 2019), which we also utilize for our first retrieval. According to Wang et al. 2019, α which is the ration of A/K_{DP} depends on differential reflectivity Z_{DR} and it monotonically decreases with increasing Z_{DR} at S-band. Further, they state "*Because rain rate estimated from the R(A) relation is roughly proportional to* α*, the algorithm inevitably tends to underestimate tropical rain or light rain in general which* *are characterized by low values of DR if a default value of a typical for continental rain is utilized."*

The second parameter is β, which according toR14 is "usually within 0.6-0.9 at microwave frequencies." Wang et al. 2019 suggested a value of 0.62 for S-band radar which we implemented for our first set of retrievals. In order to better understand how changes in α and β effect the retrievals during Harvey, we will explore the effects of different values of α and β on daily and total rainfall retrievals.

3. Comparison between gauge observed and radar estimated rainfall [mm] during Harvey

Figure 7 provides scatterplots of radar versus daily gauge accumulations for August 25-29 (panels A-E) and event total precipitation (panel F). The radar estimates include the three hybrid techniques (e.g., RC, RP and RR) and the attenuation-based method RA using α=0.015 and β=0.620, as suggested by Wang et al. 2019 and Cocks et al. 2019. The different radar/gauge pairs are denoted by their color.

The scatter plot for August 25 (panel A), which was prior to the arrival of the bulk of the Harvey's tropical precipitation and was dominated mostly by continental convection, shows that all of the retrievals provide good results with the scatter roughly along the 1:1 line for the observed rain accumulations of less than 50 mm. As the regime evolved over the August 26-29 period, the hybrid retrievals were remained quite similar but were noticeably less than both the RA and gauge accumulations. On August 27, 2017, where the gauge-averaged rainfall exceeded

400 mm, all of the hybrid retrievals significantly underestimated the gauges, while the RA retrievals agreed quite well. On August 28, 2017, where gauge-averaged rainfall still exceeded 250 mm, all of the retrievals underestimated that gauges, but RA accumulations were generally still higher than the hybrid accumulations.

Figure 8 shows a time series of 15-minute rain rates and accumulations for gauges and radar estimates. Individual 15-minute gauge accumulations are shown in the thin grey lines and indicate a large variance of rainfall over the domain. The black line is the all-gauge-averaged 15-minute rainfall, the blue, green, red and gold lines are the *area-averaged* rainfall for the radar estimates (RA, RC, RP and RR, respectively). The averaged area of these radar estimate is shown as the rectangle to the northeast of the radar location shown in Figure 2 and is bounded by longitude -95.96 to -94.93 degrees west and latitude 29.50 to 30.18 degrees north. As shown, the rainfall amounts are truly historic with gauge-observed event total of approximately 875 mm over five days. Also evident is the fact that the RA rainfall retrievals are track significantly closer to the gauge observations than do the hybrid estimators.

Figure 9 provides the area-wide radar rainfall maps for RA, RC, RP and RR in Panels A-D. Panel A shows that the RA totals were in general higher than the hybrid estimators in areas of the heaviest rainfall. Further, the ability of the RA estimator to mitigate blockage is quite evident as opposed to the hybrid estimators where significant blockage occurred in the second, third and fourth quadrants. As noted previously, we filtered gauges that were blocked in the averaging area (also shown in Fig. 2) in order to keep a level playing field. However, it should be noted that in the absence of evidence of such blocking, use of the RA estimator does mitigate the problem.

4. Sensitivity of RA retrievals to changing values of α and β

From Eqs. 2-8, there are two critical parameters used in the RA approach: α and β. The parameter α, is the net ratio of A and K_{DP} along the path (Ryshkov et al. 2014, Wang et al. 2019). The β parameter, which has been used in previous studies with values of β = 0.6 - 0.9 for microwave frequencies (R14) was shown to be highly sensitive to changes in environmental conditions and DSD characteristics. According to Wang et al. 2019, β=0.620 is appropriate for S-band radars. In order to test the sensitivity of the RA estimates to the choice of specific α and β, we generated multiple data sets for combinations of α=0.15, 0.25 and 0.50, and β =0.600-0.900 in increments of 0.050 also including β=0.620.

Figure 10a provides a bar chart of the daily and total event rainfall for gauges and radars using α=0.015. In this graph, the totals for the gauges, RC, RP, RR and the nine RA estimates (for β=0.600-0.900 in increments of 0.050, but also including b=0.620) are shown. Figures 10b-c provide similar plots, but are generated with α=0.025 and α=0.050, respectively. Note that for Figs. 10b-c, unlike Fig. 10A we did not calculate RA using β=0.620. In all three figures, a dashed horizontal line is added above the daily/total gauge accumulations as a quick visual comparison between the gauge-measured and radar-retrieved rainfall.

Examining these graphs, the following points can be made: 1) an increase in α, for a given β, results in an increased estimation of RA rainfall; 2) an increase in β, for a given α, results in a decreased estimation of RA rainfall; and, 3) an increase in α creates a larger variance in rainfall for different β. Table 1 provides quantitative comparison of rainfall accumulations using different values of α and β. As an example, for $\beta=0.600$, the total rainfall accumulated using $\alpha=0.015$, $\alpha=0.025$ and $\alpha=0.050$ was 965.9 mm, 1446.2 mm and 2243.7 mm, respectively. In other words, for $\beta=0.600$, an increase of $\alpha=0.015$ to $\alpha=0.025$ resulted in an increase in rainfall by 49.7% and an increase of $\alpha=0.025$ to $\alpha=0.050$, resulted in an increase in rainfall by 55%. Hence, rain accumulation is highly sensitive to the chosen α.

Equation 9 provides the normalized radar/gauge bias. Figure 11a provides the normalized daily and event total normalized biases between the gauge-measured and radar retrieved accumulation using a set value $\alpha=0.015$. In this figure, R is the mean radar accumulation in mm, while G is the mean gauge accumulation. In this plot, the biases for the three hybrid retrievals ("DP Methods"), as well as multiple RA retrievals using $\beta=0.600$, 0.620, 0.650, 0.700, 0.750, 0.800, 0.850 and 0.900. In general, the hybrid methods tend to underestimate the gauges, except for August 25, 2017 where they slightly overestimate them. The RA retrievals for $\beta=0.600$ and 0.620 and 0.650 all do quite well, but for $b>0.650$, the RA retrievals tend to underestimate the gauges.

$$\text{Bias} = 100\% * [R - G]/G \qquad (9)$$

Similarly, Figs 11b-c show the biases, with set values of $\alpha=0.025$ and $\alpha=0.050$, respectively. The dashed lines show that the three hybrid estimators all track quite closely to one another. However, the varying RA totals are quite variable and become more so as α increases. For $\alpha=0.015$ and $\alpha=0.025$, the minimum biases are those with β between 0.600 and 0.750; however, for $\alpha=0.050$, the lowest biases are those using β between 0.800 and 0.900. Table 2 provides the values of the radar retrieved biases relative to the gauges for the three hybrid estimates as well as multiple RA accumulations using difference values of α and β. We would like to emphasize that the point of this study isn't to find the best α, β pair for a given day, but rather to understand how different values of α and β affect the accumulations in general.

5. Changes in the DSD over the Harvey Event.

Figure 12 shows Probability Density Functions (PDF) of key radar observables, (CZ, DR, PH, which was used to calculate KD), as well as three retrieved parameters (DM, NW and RA) in panels A-F, respectively. These PDF show how these fields changed from day to day over the event. For example, on 08/25/2017, the PDF of reflectivity (Panel A) shows that CZ was substantially weaker than other days with a mode of about 27 dB, while the reflectivities on 08/27/2017 (red curve) the reflectivity mode was closer to 30-35 dB. Also, on 08/27/2017, the PDFs indicate that larger DR, KD, DM were observed compared to the other days.

Figure 13 (following Carr et al. 2017) shows a density plot comparing reflectivity (ordinate) versus differential reflectivity (abscissa). Panels A-E show the daily extraction of CZ and DR pairs over the area of interest (i.e. the rectangle above the gauges shown in Fig. 1) for August 25 – 29, 2017. The contours represent the relative percent of observed pairs over each day. To minimize noise in the data, the pairs were selected only if the $1 < CZ < 60$ dBZ, binned by 1 dB, and the $0 < DR < 4$ dB, binned by 0.25 dB. Together Figs. 12 and 13 can be used to better understand the evolving DSD from day to day and Table 3 summarizes these characteristics. On 08/25/2017, the precipitation was relatively light (average gauge rainfall of only 16.4 mm) and was associated with small CZ, DR, KD, DM and NW. Using DM as a proxy for drop size and NW as a proxy for drop counts, 08/25/2017 was dominated by a small number of small drops and thus the rain rates were relatively low. On the other hand, the precipitation on 08/27/2017 was characterized by moderate

ZH and NW and large CZ, KD and DM. Hence, this day was dominated by a moderate to large number of large drops, resulting in very large rain rates: average gauge rainfall was in excess of 400 mm. By 08/28/2017, the precipitation was dominated by a large number of moderate sized drops, resulting in another very heavy rain event with average gauge rainfall in excess of 200 mm.

Figure 14 illustrates how the hybrid retrievals (here proxied by the RC retrieval) were affected by the changing CZ, DR and KD environments by providing a time series of the specific method invoked on a scan-to-scan basis. In the RC method, there are four methods invoked to retrieve the rain rate from a set of observations of CZ, DR and KD. See Fig. 4 for the specific values needed to trigger a given method. Figure 14 then gives the percentage of pixels in each scan that a particular method was invoked. On 8/25/2017, where the pre-storm precipitation was mostly continental convection, the Z_H-only (brown) method was invoked about 60% of the time and the remainder of the points used the Z_H+Z_{DR} (gold) method. By 08/26/2017 between 1000-2000 UTC, as the storm settled to the west of Houston, Z_H+K_{DP} was utilized up to about 15% of the time, while Z_H+Z_{DR} and Z_H were invoked approximately 60% and 25% of the time, respectively. On August 27, 2017, which is the period where the bulk of the event rainfall fell, the Z_{DR}+K_{DP} was utilized as much as 30% of the time and the Z_H+Z_{DR} method was used as much as 75% of the time. This is indicative of large Z_H, Z_{DR} and K_{DP}. In other words, this was probably the result of the presence of a large number of large drops in the DSD resulting in extremely heavy rainfall. By 08/28/2017, the regime seems to have changed such that a large number of small drops were present, typical of tropical cyclone DSD characteristics (Tokay et al. 2008). This change may be due to drop sorting by the stronger winds that were present on this day. Recent research has shown that wind effects can affect the DSD. Testik and Pei 2017 found that increasing wind speeds modified the DSD by increasing the number of small drops and decreasing the number of large drops via collisional drop breakup. Figure 15 provides the series of wind speeds and direction observed at Houston Intercontinental Airport (KIAH in Fig. 2). While the center of Harvey was located well west of Harris County for much of the time, wind speeds were on the order of 15-20 kts during August 25-26, 2017, but did increase some during August 28-29. To be sure, this DSD regime still provided significant rainfall, but not as high as that on August 27, 2017. On 08/25/2017, where Z_H, Z_{DR} and K_{DP} were in general relatively small had the lowest accumulations. On 08/27/2017 Z_H was moderate, while Z_{DR} and K_{DP} were large, resulting in a large number of large drops and intense rainfall. By 08/29/2017, Z_H was moderate, while Z_{DR} and K_{DP} were small, resulting in only moderate (relatively speaking) rainfall.

6. Summary and Conclusions

A comparison of several dual-polarization radar retrievals versus rain gauges was performed over Houston, Texas during the five-day Hurricane Harvey flooding event (August 25-29, 2017). The radar data used in this study were obtained from the KGHX WSR-88D radar located in League City, TX which is southeast of Houston, TX. The radar operated continuously throughout the five-day event. To provide quality control (QC) of the KHGX data, we employed the dual-polarimetric quality control (DPQC) procedures applied to radar data as those routinely generated by the Global Precipitation Measurement (GPM) mission Ground Validation (GV) Program (Petersen et al., 2019; cf details for DPQC in Pippitt et al., 2015, Marks et al. 2011). Specifically, GPM GV adapted a series of algorithms based on Ryzhkov et al. 1998 for conducting DPQC. The DPQC algorithms are successful in identifying and removing non-precipitating echoes (Ryzhkov and Zrnic 1998; Zrnic and Ryzhkov 1999; Cifelli et al. 2002).

The reference data set utilized 120 rain gauges that are part of the Harris County Flood Warning System (HCFWS); however, due to some limited radar blockage over the network, and additional 21 of the 120 gauges were removed from the analysis.

The radar rain retrievals were from three common hybrid techniques: Cifelli et al. 2011 (RC); Bringi et al. 2009 (RP); and Chen et al. 2017 (RR), and a fourth estimator that utilizes an attenuation-base method provided by Ryzhkov et al. 2014 was also used (RA).

There are two key parameters introduced utilized by the RA method: α which is the coefficient of the Path Integrate Attenuation (PIA) described by other (Meneghini and Nakamura 1990; Iguchi and Meneghini 1994, Testud et al. 2000, Bringi et al. 1990); and, β which has been used in previous studies with values of β = 0.6-0.9 for microwave frequencies (Ryzhkov et al. 2014). It was shown that both α and β are highly sensitive to the DSD of the precipitation. According to Wang et al. 2019, β=0.620 is appropriate for S-band radars. In order to test the sensitivity of the RA estimates to the choice of specific α and β, we generated multiple data sets for combinations of α=0.15, 0.25 and 0.50, and β =0.600-0.900 in increments of 0.050. As an example, for β=0.600, the total rainfall accumulated using α=0.015, α=0.025 and α=0.050 was 965.9 mm, 1446.2 mm and 2243.7 mm, respectively. In other words, for β=0.600, an increase of α=0.015 to α=0.025 resulted in an increase in rainfall by 49.7% and an increase of α=0.025 to α=0.050, resulted in an increase in rainfall by 55%. Hence, rain accumulation is highly sensitive to the chosen α.

The results of this analysis showed the following: 1) an increase in α, for a given β, results in an increased estimation of RA rainfall; 2) an increase in β, for a given α, results in a decreased estimation of RA rainfall; and, 3) an increase in α creates a larger variance in rainfall for different β. Wang et al. 2019 and Cocks et al. 2019 suggest a method for determining an α on a scan-by-scan basis using a β=0.620. The differences in the ambient DSD characteristics made setting a constant value of α and β difficult. And, unfortunately, there was no *in situ* DSD data available for Harvey, so we had to rely on the radar observables to deduce how the DSD changed over the course of the event. To do so, we utilized probably distributions of observed reflectivity, differential reflectivity, and the differential phase, which was used to calculate the specific differential phase. We also examined the PDFs of retrieved DSD parameters including mass weight mean diameter DM, the normalized intercept NW and rain rate.

Density plots comparing reflectivity versus differential reflectivity showed the daily extraction of CZ and DR pairs over the area for August 25 – 29, 2017. The contours represent the relative percent of observed pairs over each day. To minimize noise in the data, the pairs were selected only if the $1 < CZ < 60$ dBZ, binned by 1 dB, and the $0 < DR < 4$ dB, binned by 0.25 dB. On 08/25/2017, the precipitation was relatively light (average gauge rainfall of only 16.4 mm) and was associated with small CZ, DR, KD, DM and NW. Using DM as a proxy for drop size and NW as a proxy for drop counts, 08/25/2017 was dominated by a small number of small drops and thus the rain rates were relatively low. On the other hand, the precipitation on 08/27/2017 was characterized by moderate CZ and NW and large DR, KD and DM. Hence, this day was dominated by a moderate to large number of large drops, resulting in very large rain rates: average gauge rainfall was in excess of

400 mm. By 08/28/2017, the precipitation was dominated by a large number of moderate sized drops, resulting in another very heavy rain event with average gauge rainfall in excess of 200 mm.

Each of the hybrid techniques base their point-by-point retrievals on observed values of CZ, DR and KD. In order to illustrate which particular method we developed time of the percentage of points for a given scan that is employed by a given method. Figure 14 illustrates how the hybrid retrievals (here proxied by the RC retrieval) were affected by the changing CZ, DR and KD environments by providing a time series of the specific method invoked on a scan-to-scan basis. In the RC method, there are four methods invoked to retrieve the rain rate from a set of observations of CZ, ZD and KD. Figure 11 then gives the percentage of pixels in each scan that a particular method was invoked. On 8/25/2017, where the pre-storm precipitation was mostly continental convection, the Z_H-only (brown) method was invoked about 60% of the time and the remainder of the points used the Z_H+Z_{DR} (gold) method. By 08/26/2017 between 1000-2000 UTC, as the storm settled to the west of Houston, Z_{DR}+K_{DP} was utilized up to about 15% of the time, while Z_H+Z_{DR} and Z_H were invoked approximately 60% and 25% of the time, respectively. On August 27, 2017, which is the period where the bulk of the event rainfall fell, the Z_{DR}+K_{DP} was utilized as much as 30% of the time and the Z_H+Z_{DR} method was used as much as 75% of the time. This is indicative of large Z_H, Z_{DR} and K_{DP}. In other words, this was probably the result of the presence of a large number of large drops in the DSD resulting in extremely heavy rainfall. By 08/28/2017, the regime seems to have changed such that a large number of small drops were present, typical of tropical cyclone DSD characteristics (Tokay et al. 2008). This change may be due to drop sorting by the stronger winds that were present on this day. Recent research has shown that wind effects can affect the DSD. Testik and Pei 2017 found that increasing wind speeds modified the DSD by increasing the number of small drops and decreasing the number of large drops via collisional drop breakup. Figure 15 provides the series of wind speeds and direction observed at Houston Intercontinental Airport (KIAH in Fig. 2). While the center of Harvey was located well west of Harris County for much of the time, wind speeds were on the order of 15-20 kts during August 25-26, 2017, but did increase some during August 28-29. To be sure, this DSD regime still provided significant rainfall, but not as high as that on August 27, 2017. Table 4 illustrates how the bulk statistics of CZ, DR and KD from day-to-day correspond to the intensity of the retrieved rain rates. On 08/25/2017, where CZ, DR and KD were in general relatively small had the lowest accumulations. On 08/27/2017 CZ was moderate, while DR and KD were large, resulting in a large number of large drops and intense rainfall. By 08/29/2017, CZ was moderate, while DR and KD were small, resulting in only moderate (relatively speaking) rainfall.

These results suggest that there are large differences in the RA rain rate retrievals that are highly influenced by changing the ambient DSD. Wang et al. 2019 and Cocks et a. 2019 suggest a method for specifying an alpha on a scan-by-scan basis using a b=0.620. We did not invoke this procedure in this study because our emphasis was to examine the sensitivity of rain retrievals to changes in a and b. However, we do recognize that such techniques do need to be employed to make RA estimates more robust and will continue to investigate techniques to improve rain retrievals for GPM GV.

Acknowledgements

We would like to thank Dr. Gail Skofronick-Jackson for her support as the previous GPM Project Scientist and current Program Scientist. This study was funded through the NASA Precipitation Measurement Mission and the GPM Ground Validation program.

References

Atlas D., and C. W. Ulbrich, 1977: Path- and area-integrated rainfall measurement by microwave attenuation in the 13cm band. *J. Appl. Meteor.*, **16**, 1322-1331.

Blake and Zelinsky, 2018. National Hurricane Center Tropical Cyclone Report: Hurricane Harvey (AL092017). https://www.nhc.noaa.gov/data/tcr/AL092017_Harvey.pdf

Brandes, E. A., G. Zhang, and J. Vivekanandan, 2002: Experi- ments in rainfall estimation with a polarimetric radar in a sub- tropical environment. J. Appl. Meteor., 41, 674–685.

Bringi V. N., V. Chandrasekar, N. Balakrishnan, and D. S. Zrnic, 1990: An examination of propagation effects in rainfall on polarimetric variables at microwave frequencies. *J. Atmos. Oceanic Tech*., **7**, 829-840.

Bringi V. N., T.Tang, and V. Chandrasekar, 2004: Evaluation of a New Polarimetrically Based Z–R Relation. *J. Atmos. and Ocean. Tech*., **21**, 612-623.

Carr N., P. E. Kirstetter, J. J. Gourley and Y. Hong, 2017: Polarimetric Signatures of Midlatitude Warm-Rain Precipitation Events, J. Appl. Meteor. Clim. 56, 697-711.

Chen H., V. Chandresakar and R. Bechini, 2017: An Improved Dual-Polarization Radar Rainfall Algorithm (DROPS2.0): Application in NASA IFloodS Field Campaign, *Jou. Hydromet*. **18**, 917-937.

Cifelli, R., W. A. Petersen, L. D. Carey, S. A. Rutledge, and M. A. F. da Silva Dias, 2002: Radar observations of the ki- nematic, microphysical, and precipitation characteristics of two MCSs in TRMM LBA. J. Geophys. Res., 107, 8077, doi:10.1029/ 2000JD000264.

Cifelli R., V. Chandrasekar, S. Lim, P. Kennedy, Y. Wang, and S. Rutledge, 2011: A new dual-polarization radar rainfall algorithm: Application in Colorado precipitation events. *J. Atmos. Oceanic Technol.,* **28**, 352-364.

Cocks, S. B., L. Tang, P. Zhang, A. Ryzhkov, B. Kaney and K. L. Elmore Y. Wang, J. Zhang and K. Howard, 2019: A Prototype Quantitative Precipitation Estimation Algorithm for Operational S-Band Polarimetric Radar Utilizing Specific Attenuation and Specific Differential Phase. Part II: Performance Verification and Case Study Analysis. *Jou. Hydromet*., 20, 999-1014.

Giangrande, S., and A. Ryzhkov, 2008: Estimation of rainfall based on the results of polarimetric echo classification. J. Appl. Meteor., 47, 2445–2462, https://doi.org/10.1175/ 2008JAMC1753.1.

Hou A. Y., R. K. Kakar, S. Neeck, A. A. Azarbarzin, C. D. Kummerow, M. Kojima, R. Oki, K. Nakamura and T. Iguchi, 2014: The Global Precipitation Measurement Mission. *Bull. Amer. Met. Soc.,* **95**, 701-722.

Iguchi T., and R. Meneghini, 1994: Intercomparison of single frequency methods for retrieving a vertical rain profile from airborne or spaceborne radar data. *J. Atmos. Ocean. Tech*., **11**, 1507-1516.

Meneghini R., and K. Nakamura, 1990: Range profiling of the rain rate by an airborne weather radar. Remote Sens. Environ., **31**, 193-209.

Pippitt, J. L., D. A. Marks, and D. B. Wolff, 2013: Dual-polarimetric quality control for NASAs Global Precipitation Measurement (GPM) mission ground validation program. *36th AMS Conference on Radar Meteorology*, Breckenridge, CO, September 16-20, 2013.

Ryzhkov, A., and D. S. Zrnić, 1995: Comparison of dual- polarization radar estimators of rain. *J. Atmos. Ocean. Tech.*, **12**, 249–256.

Ryzhkov A., M. Diederich, P. Zhang and C. Simmer, 2014: Potential Utilization of Specific Attenuation for Rainfall Estimation, Mitigation of Partial Beam Blockage, and Radar Networking. *J. Atmos. Ocean. Tech.,* **31**, 599-619.

Ryzhkov A. V., S. E. Giangrande and T. J. Shurr, 2005: Rainfall Estimation with a Polarimetric Prototype of WSR-88D. *J. App. Meteor*., **44**, 502-515.

Ryzhkov A. V and D. Zrnic, 1998a: Beamwidth Effects on the Differential Phase Measurements of Rain. *J. Atmos. Ocean. Tech.* **15**, 624-634.

Ryzhkov A. V. and D. S. Zrnic, 1998b: Polarimetric rainfall estimation in the presence of anomalous propagation. J. Atmos. Ocean. Tech., 15, 1320–1330.

Schwaller M. R. and K. R. Morris, 2011: A Ground Validation Network for the Global Precipitation Measurement Mission. *J. Atmos. Ocean. Tech.,* **28**, 301-319.

Seo B-C, W. F. Krajewski, F. Quintero, M. ElSaadani, R. Goska, L. K. Cunha, B. Dolan, D. B. Wolff, J. A. Smith, S. A. Rutledge, W. A. Petersen, 2018: Comprehensive Evaluation of the IFloodS Radar Rainfall Products for Hydrological Applications. *J. Hydro. Met.*, **19**, 1793-1812.

Testik F. Y. and B. Pei, 2017: Wind Effects on the Shape of Raindrop Size Distribution, *J. of Hydromet*., **18**, 1285-1303.

Testud J., E. Le Bouar, E. Obligis, and M. Ali-Mehenni, 2000: The rain profiling algorithm applied to polarimetric weather radar. *J. Atmos. Ocean. Tech.,* **17**, 332-356.

Tokay A. P. G. Bashor, E. Habib and T. Kasparis, 2008: Raindrop size distribution measurements in tropical cyclones. *Mon. Wea. Review*, **136**, 1669-1686.

Tokay A., L. P. D'Adderio, D. B. Wolff, W. A. Petersen, 2019: Development of Raindrop Size Distribution Parameters for the NASA Global Precipitation Measurement Mission Ground Validation Program. *J. Atmos. Ocean. Tech., Submitted.*

Wang Y., and V. Chandrasekar, 2009: Algorithm for estimation of the specific differential phase. *J. Atmos. Ocean. Tech.*, **26**, 2565-2578.

Wang, Y., J. Zhang, A. V. Ryzhkov, and L. Tang, 2013: C-band polarimetric radar QPEs based on specific differential propagation phase for extreme typhoon rainfall. J. Atmos. Oceanic Technol., 30, 1354–1370.

Wang, Y., S. Cocks, L. Tang, A. Ruzhkov, P. Zhang, J. Zhang, and K. Howard, 2019: A Prototype Quantitative Precipitation Estimation Algorithm for Operational S-Band Polarimetric Radar Utilizing Specific Attenuation and Specific Differential Phase. Part I: Algorithm Description. *Jou. Hydromet*., 20, 985-997.

Zrnic, D. S., and A. V. Ryzhkov, 1999: Polarimetry for weather surveillance radars. *Bull. Amer. Met. Soc.,* **80**, 389-406.

Figures

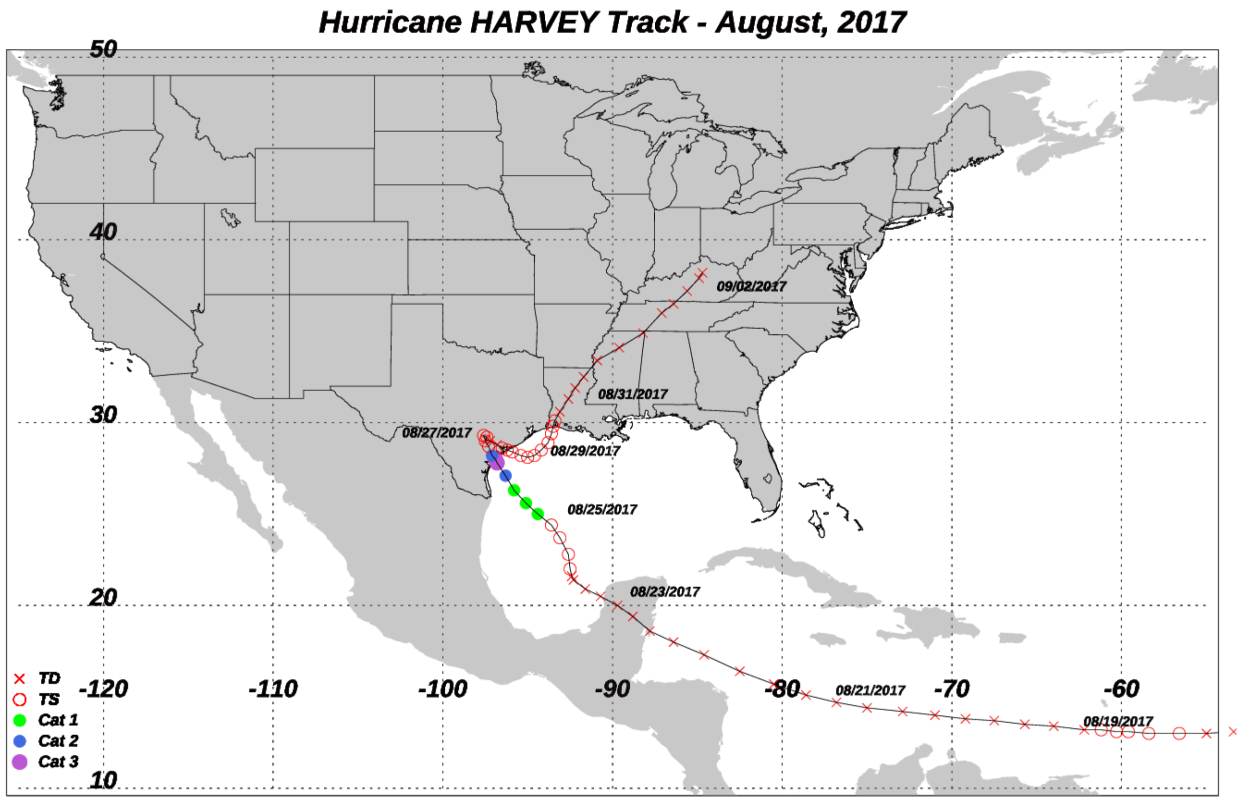

Fig. 1: Hurricane Harvey track generated using National Hurricane Center “Best Track” data.

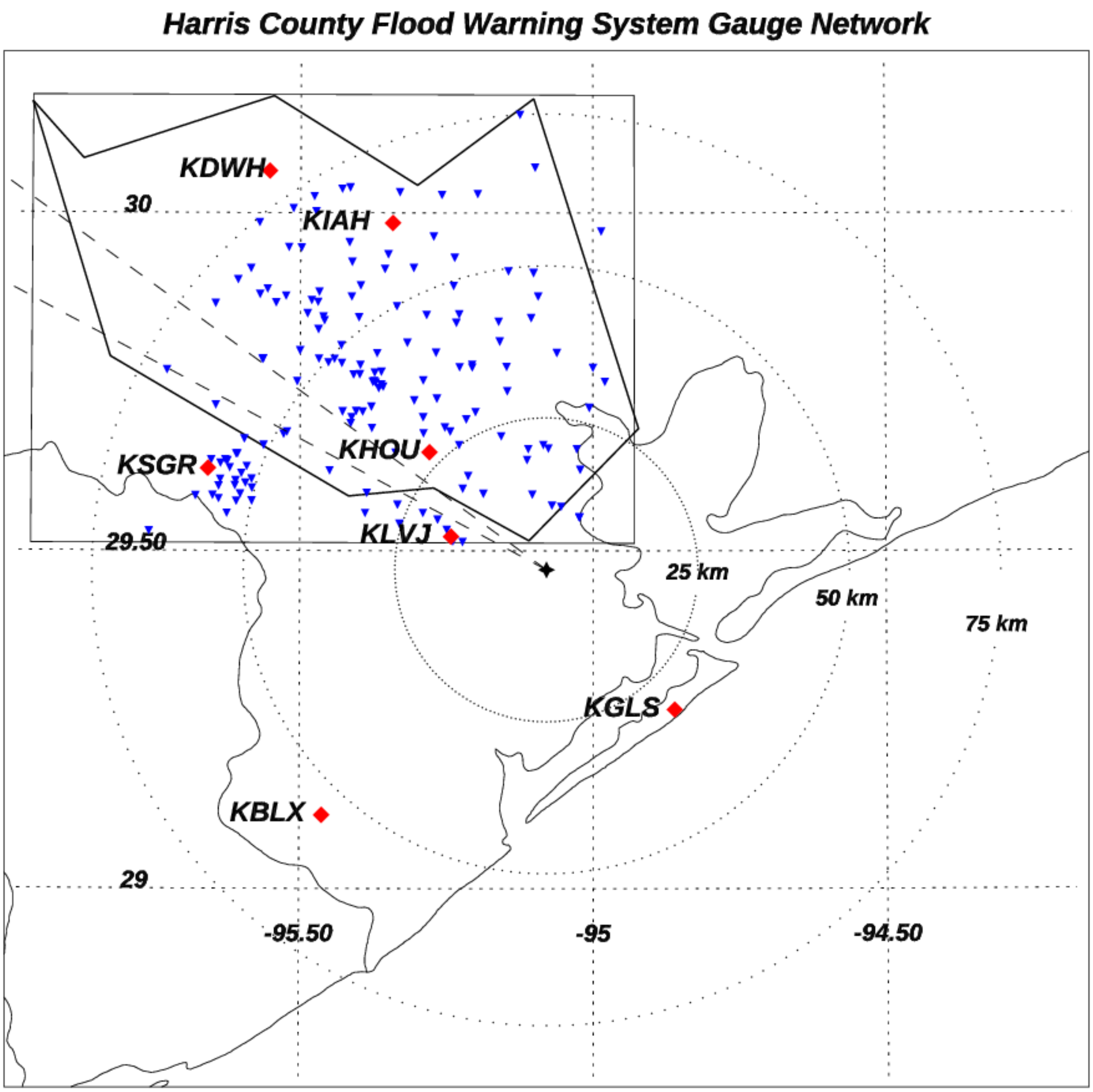

Fig. 2: Map of the Harris County Flood Warning System (HCFWS) network of rain gauges. The rectangle to the top left is the averaging area used for computing means and profiles. The polygon within the rectangle is a rough outline of Harris County, TX. Of the 120 gauges within the area, 21 were removed due to known blockage between 298° and 306° from the radar (the area between the dashed lines). The red diamonds represent locations where National Weather Service Automated Surface Observations System (ASOS) sites are located and local wind data is analyzed.

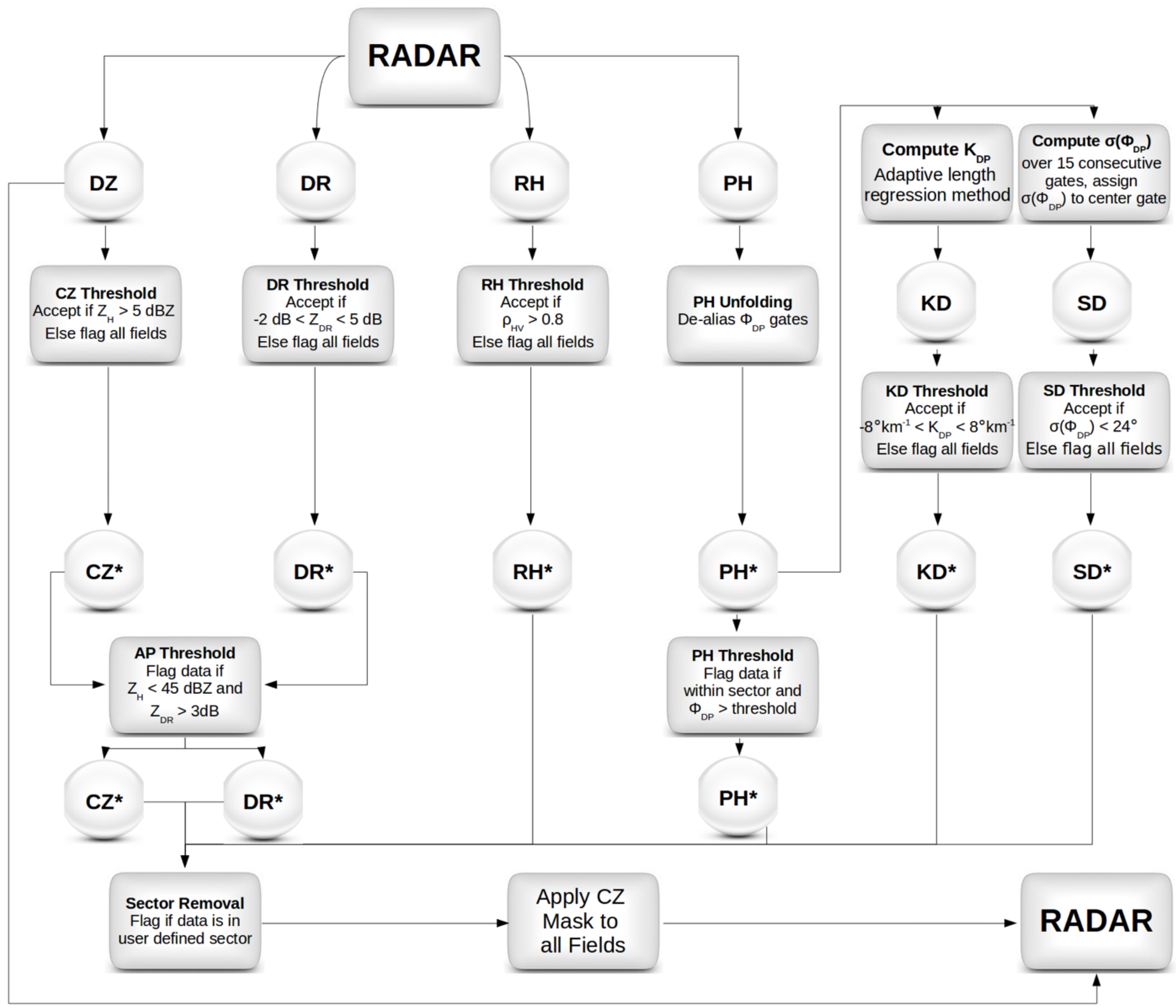

* All fields are modified in each step to remove non-precipitating echo. Threshold values are default for WSR-88D radars.

Fig. 3: Flowchart of the Dual-Polarization Quality Control (DPQC) stream used by the GPM Ground Validation (GV) group, as adapted from Ryzhkov et al. 1998.

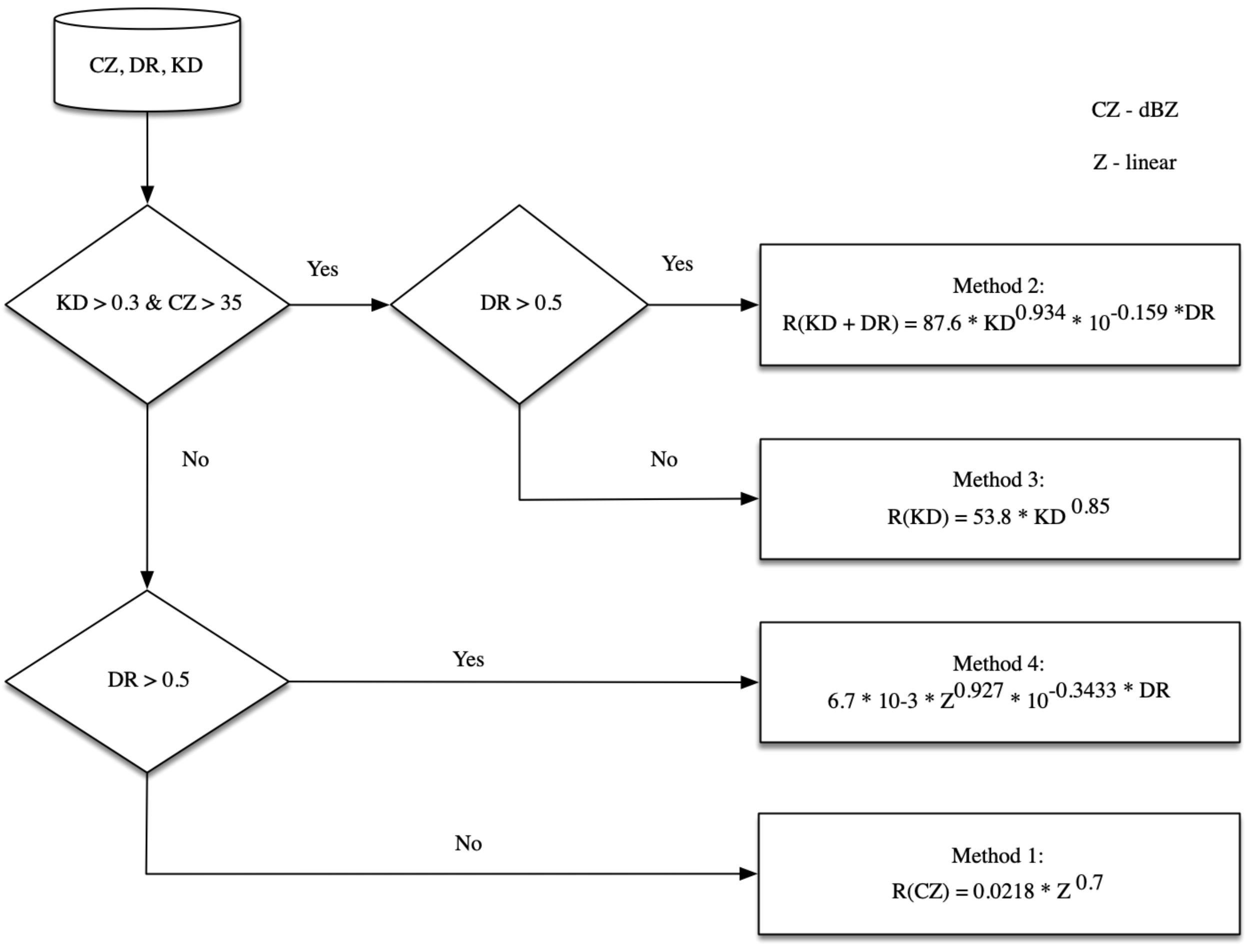

Fig. 4: Flowchart of the hybrid dual-polarization rain retrieval developed by Cifelli et al. 2011.

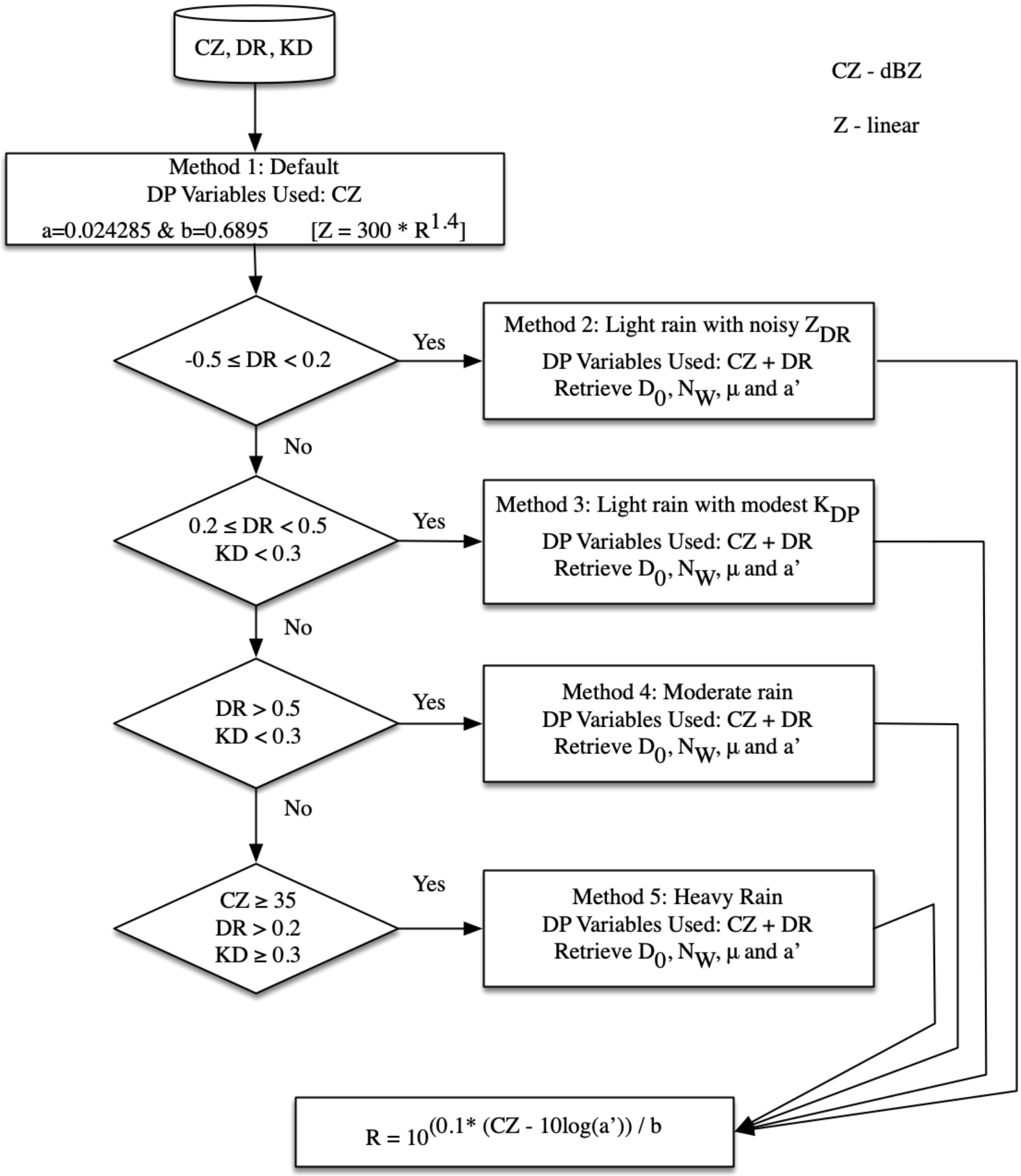

Fig. 5: Same as Fig. 4 except adapted from Bringi et al. 2004.

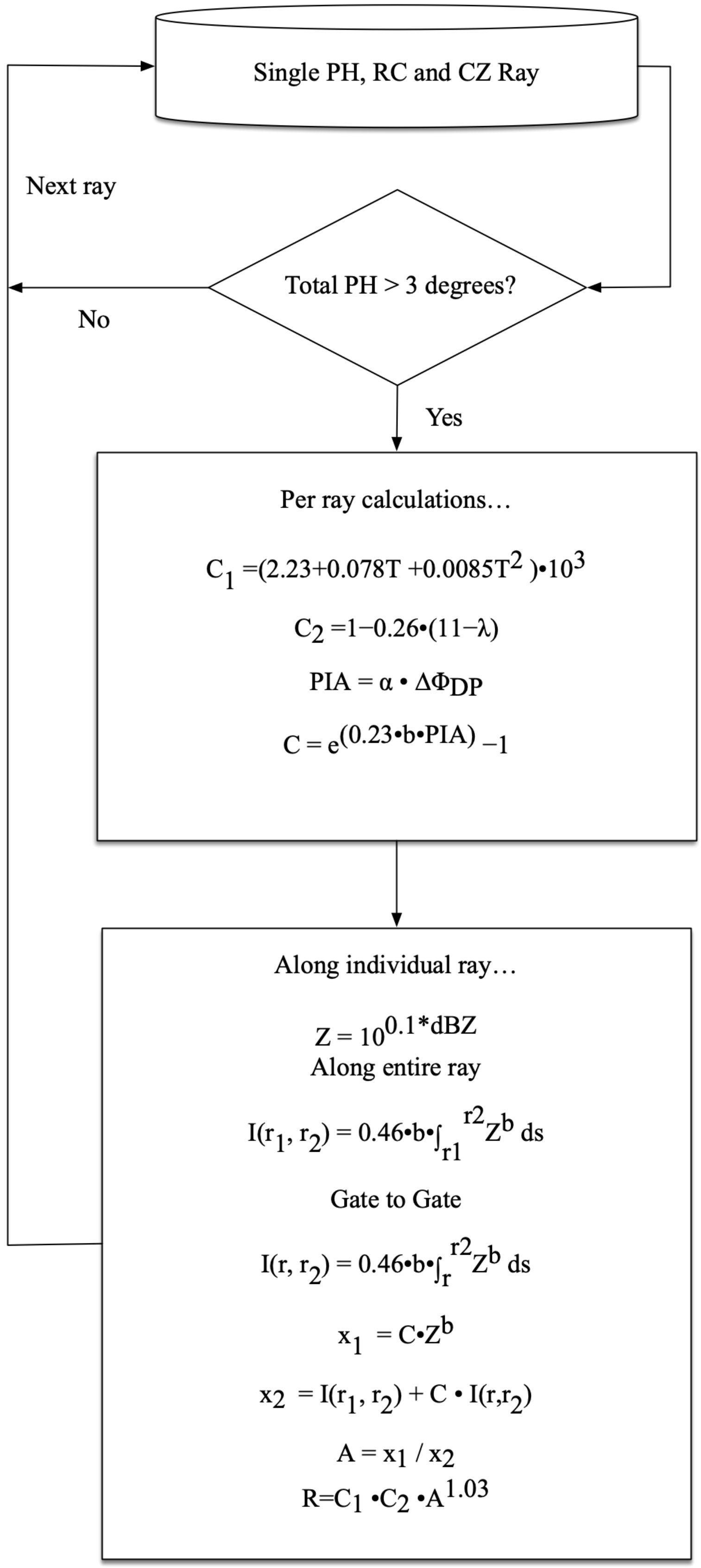
Single PH, RC and CZ Ray
Next ray
Total PH > 3 degrees?
No
Yes
Per ray calculations…
$C_1 = (2.23+0.078T+0.0085T^2)\bullet 10^3$
$C_2 = 1-0.26\bullet(11-\lambda)$
$PIA = \alpha \bullet \Delta\Phi_{DP}$
$C = e^{(0.23\bullet b\bullet PIA)} - 1$
Along individual ray…
$Z = 10^{0.1*dBZ}$
Along entire ray
$I(r_1, r_2) = 0.46\bullet b\bullet\int_{r1}^{r2} Z^b\, ds$
Gate to Gate
$I(r, r_2) = 0.46\bullet b\bullet\int_{r}^{r2} Z^b\, ds$
$x_1 = C\bullet Z^b$
$x_2 = I(r_1, r_2) + C \bullet I(r, r_2)$
$A = x_1 / x_2$
$R = C_1 \bullet C_2 \bullet A^{1.03}$

Fig. 6: Flowchart of the attenuation-based dual-polarization rain retrieval by Ryzhkov et al. 2014. The reflectivity Z is in units of $mm^6 mm^{-3}$. The temperature T corresponds to the temperature at the height of the beam at a given radar gate and was retrieved from hourly Rapid Update Cycle (RUC) model output (https://rucsoundings.noaa.gov).

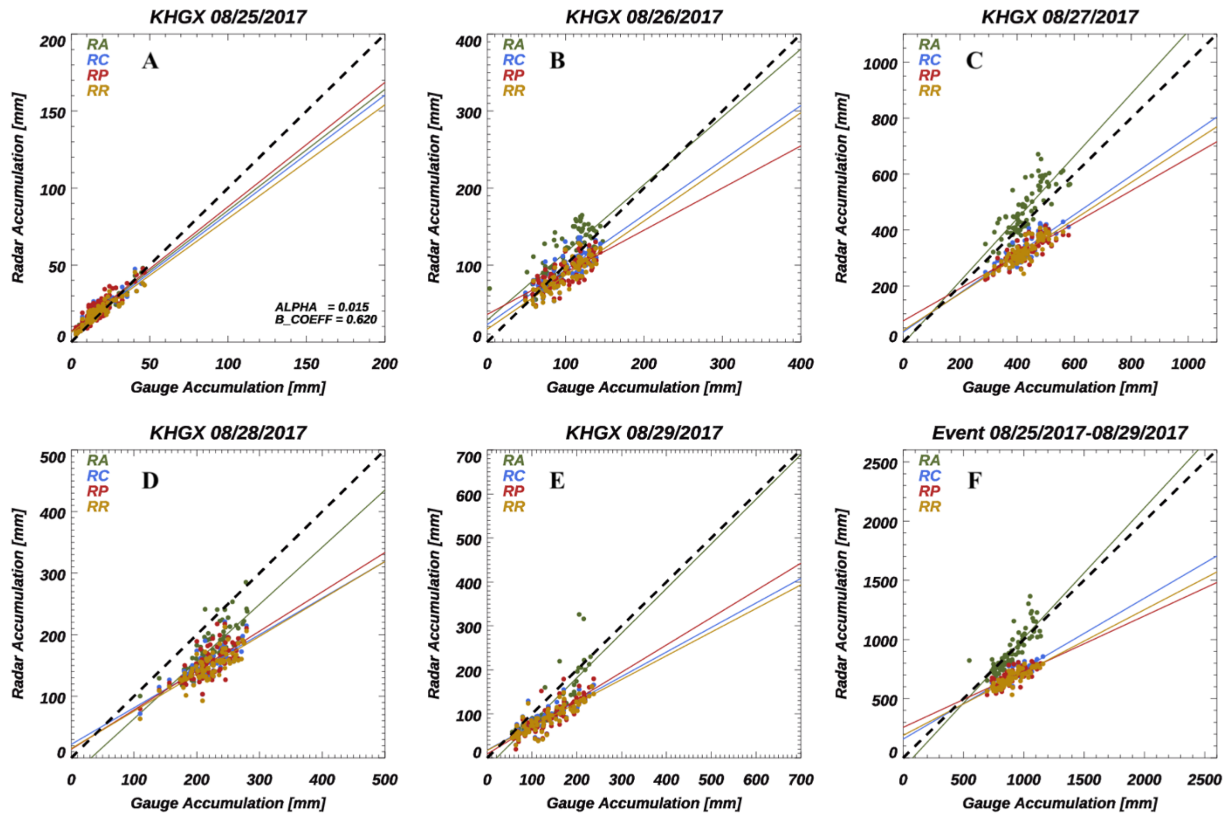

Fig. 7: Scatterplot of radar versus gauge daily and total rain accumulations [mm] using α=0.015 and β=0.620. The different rain estimates are color coded: RA (green); RC (blue); RP (red); and, RR: golden). The colored lines are linear regression lines between the gauge accumulations and each estimator and are denoted by the colored text in the top left of each panel.

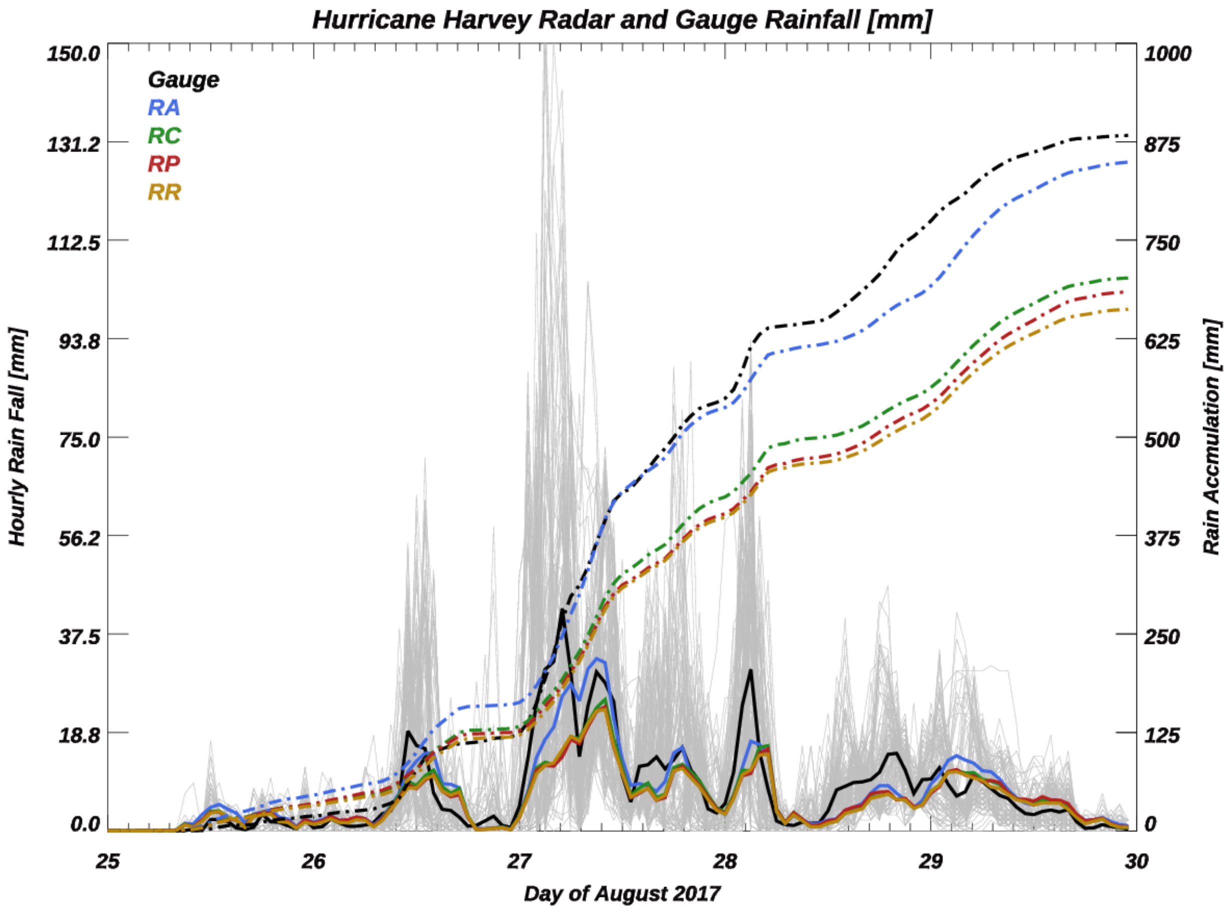

Fig. 8: Time series of 15-minute rainfall accumulations from gauges and radar estimators. The light gray series show 15-minute rain accumulations from individual gauges, while the thick black line represents the 15-minute mean from all gauges. The radar estimators are color coded according to the legend (RA-blue; RC-green; RP-red; and RR: goldenrod). As is evident, the RA estimator (α=0.015 and β=0.620) significantly out-performed the hybrid estimators over the entirety of the event.

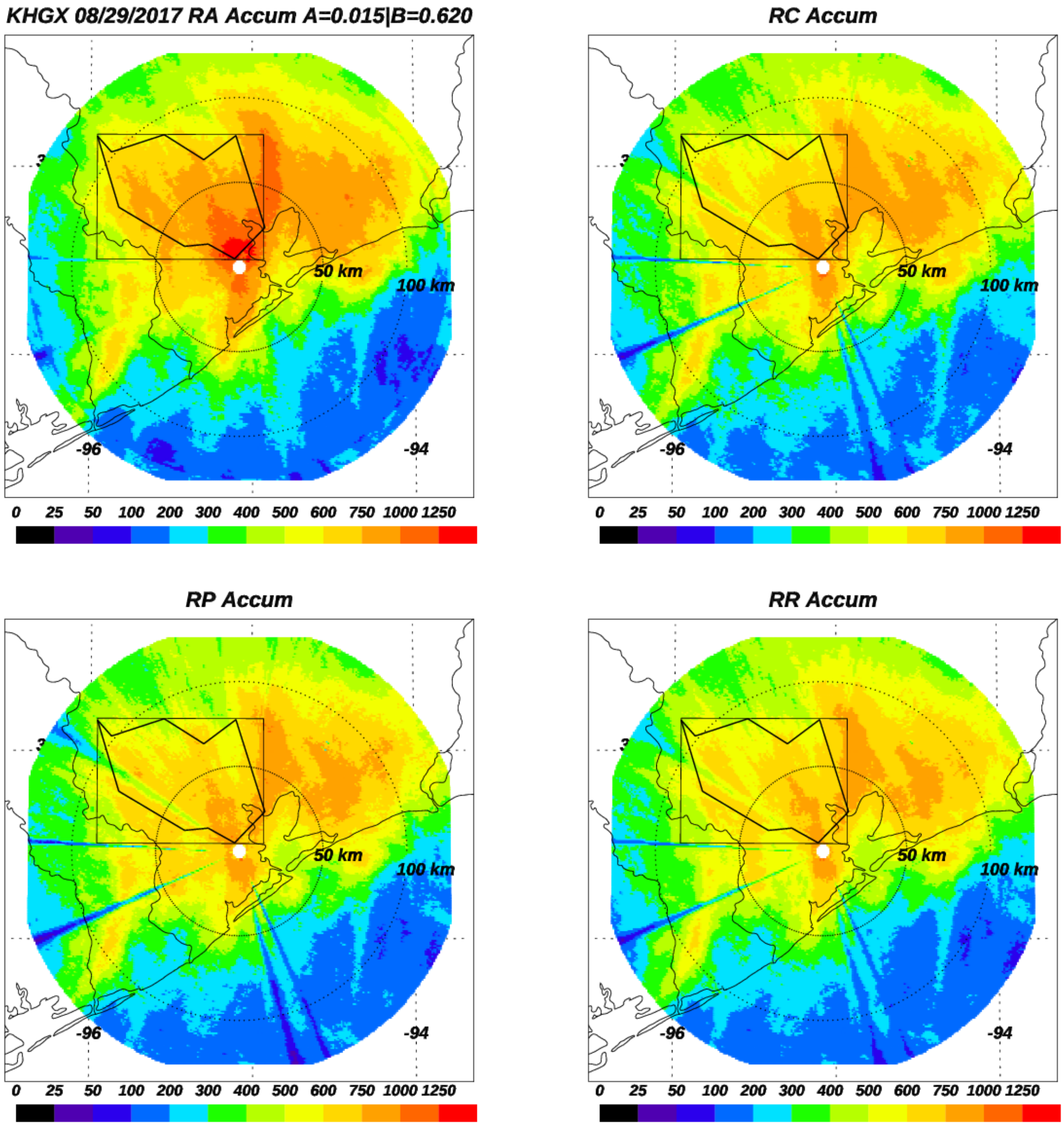

Fig. 9: Maps showing total accumulation from Hurricane Harvey over the period 08/25/2017 – 08/29/2017. Top left panel shows RA accumulations (A=α=0.015; B=β=0.620). Top right, bottom left and bottom right panels show accumulations for RC, RP and RR over the same period. Of particular note is the lack of blockage in the RA estimates, relative to all of the hybrid estimates.

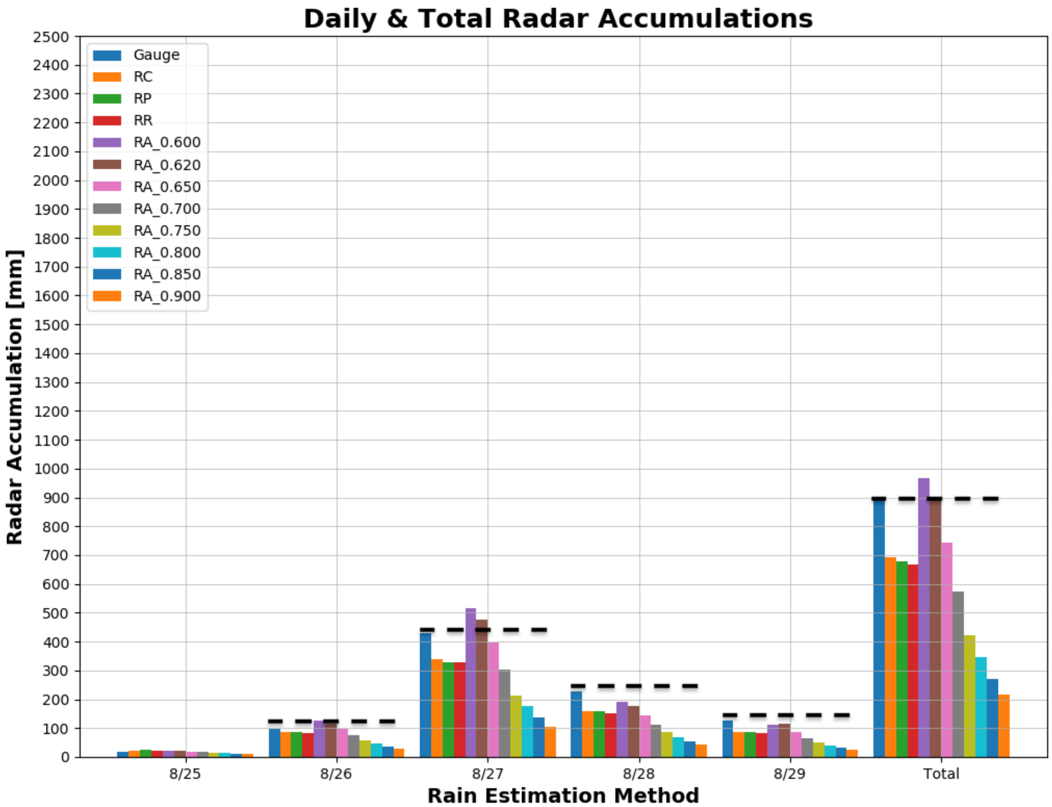

Fig. 10a: Daily and total rainfall accumulations for gauges and all radar estimators, including the three hybrid estimators (RC, RP and RR) as well as RA with α=0.015 and β=0.600, 0.650, 0.700, 0.750, 0.750, 0.800, 0.850 and 0.900. The horizontal dashed line represents that gauge measured rainfall for each period and is provided as a visual reference. The large differences between the various RA estimates illustrates well the significant dependence of β on the attenuation-based rain retrieval.

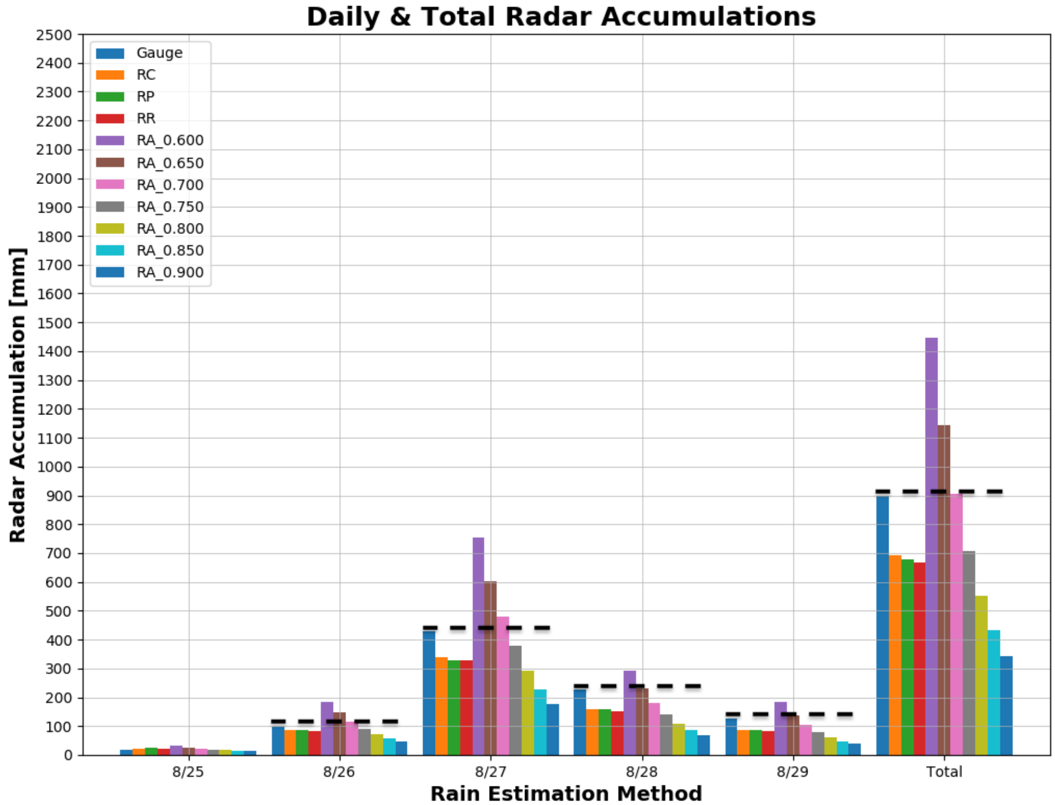

685

686 Fig. 10b: Same as Fig. 10a except for α=0.025.

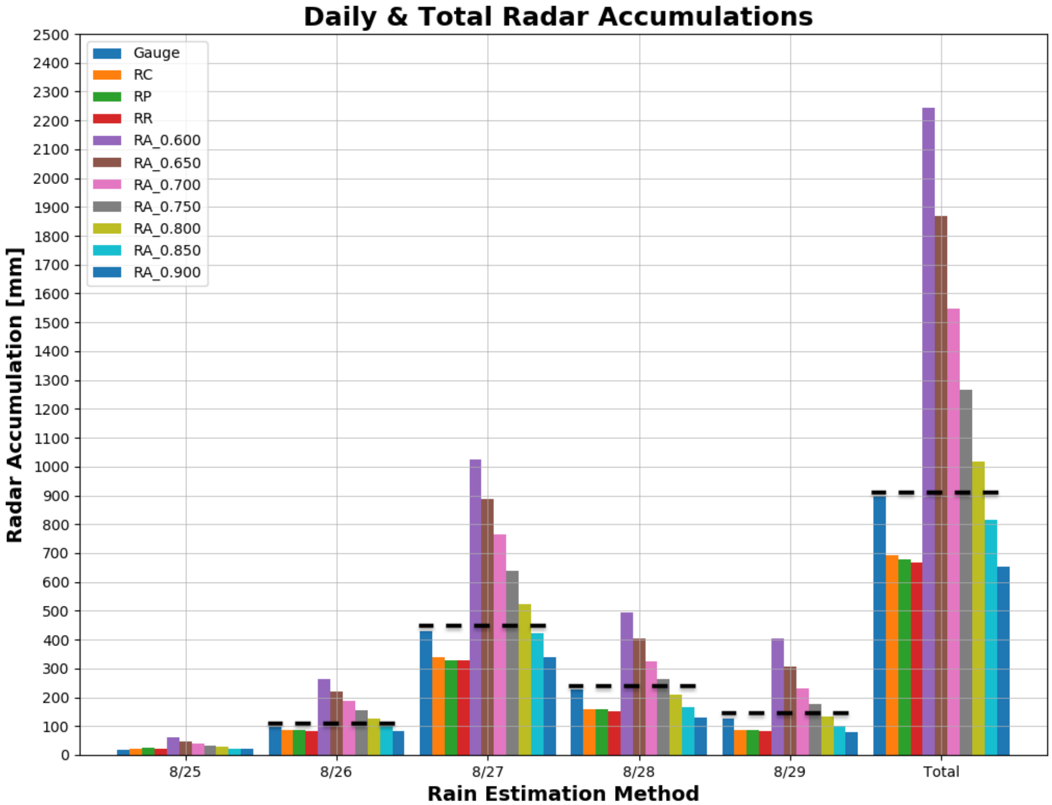

Fig. 10c: Same as Fig. 10a except for α=0.050.

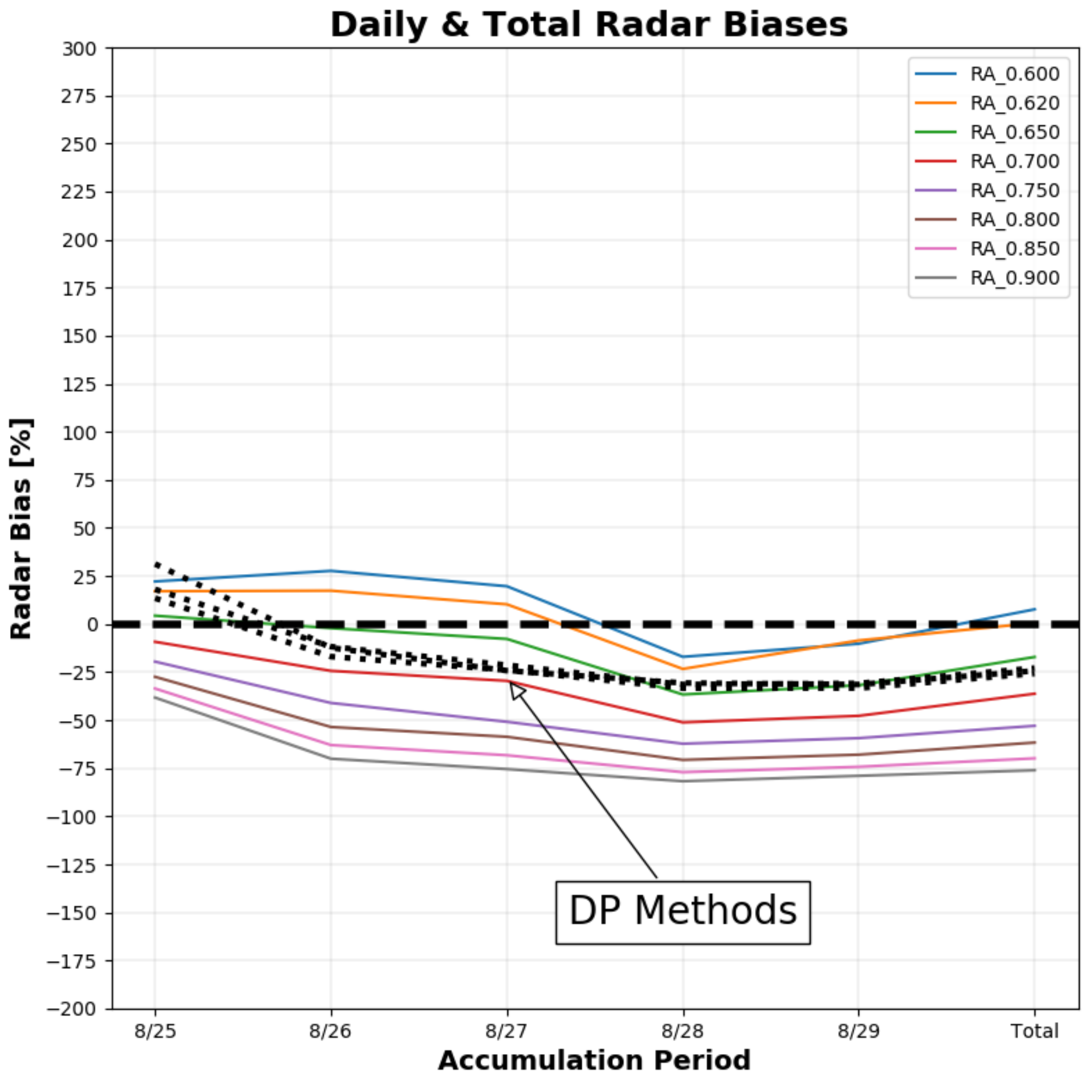

Fig. 11a: Daily and total rainfall bias between gauges and all radar estimators: the three hybrid estimators (RC, RP and RR) and the RA with α=0.015 and β=0.600, 0.620, 0.650, 0.700, 0.750, 0.800, 0.850, and 0.900. The “DP Methods” biases are shown as the black dotted lines.

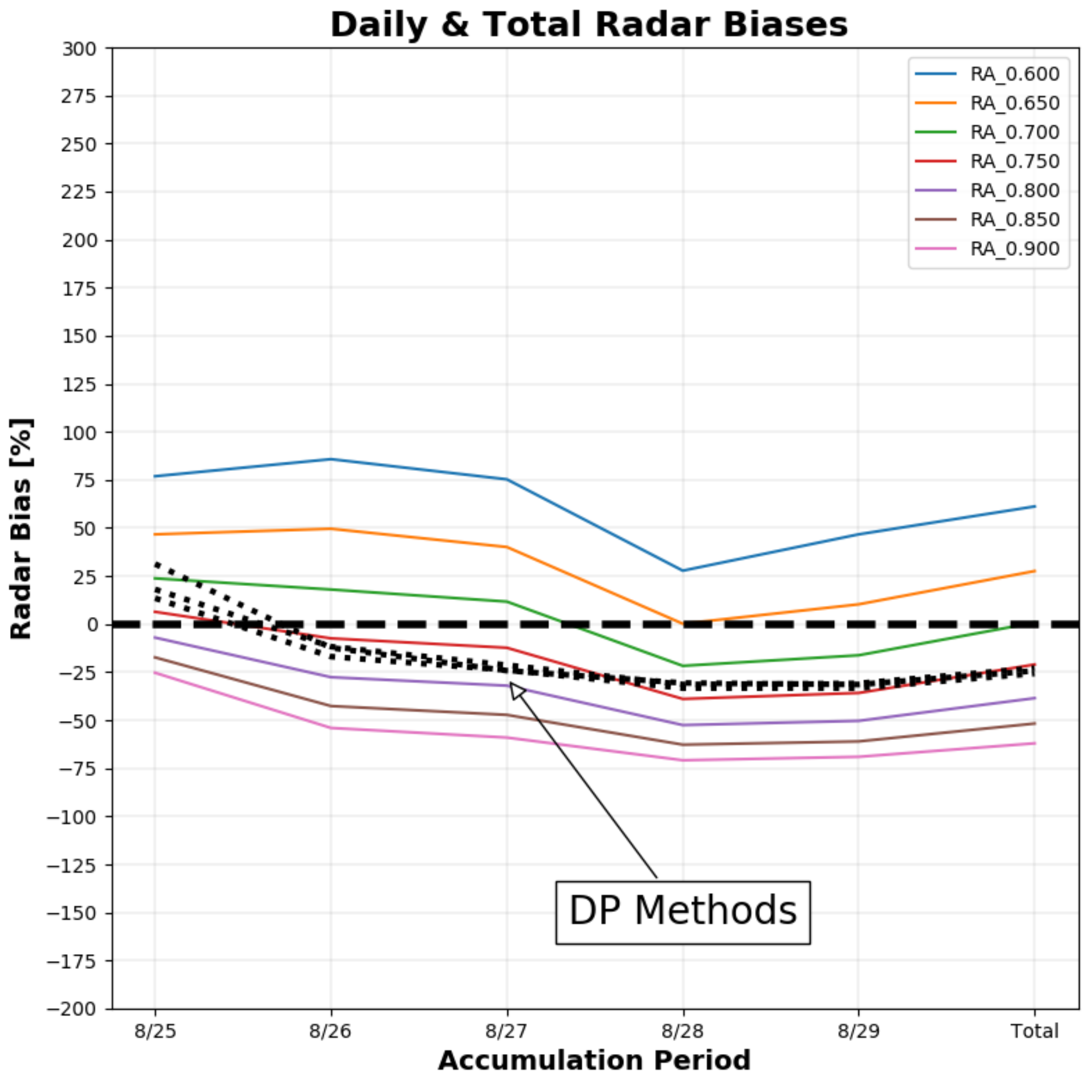

Fig. 11b: Same as Fig. 11a, except a=α=0.025 and β=0.600, 0.650, 0.700, 0.750, 0.800, 0.850, and 0.900.

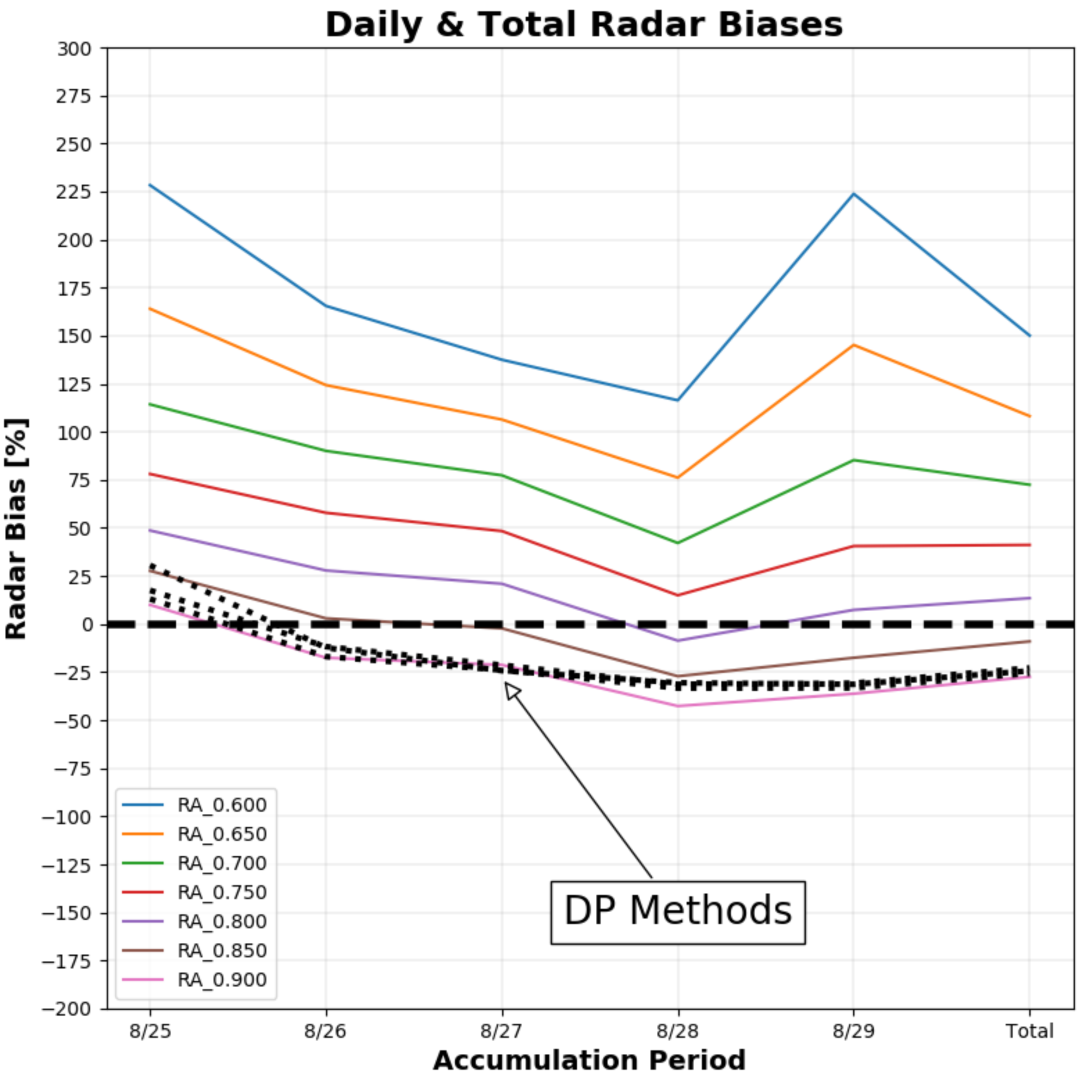

Fig. 11c: Same as Fig. 11b, except α=0.050.

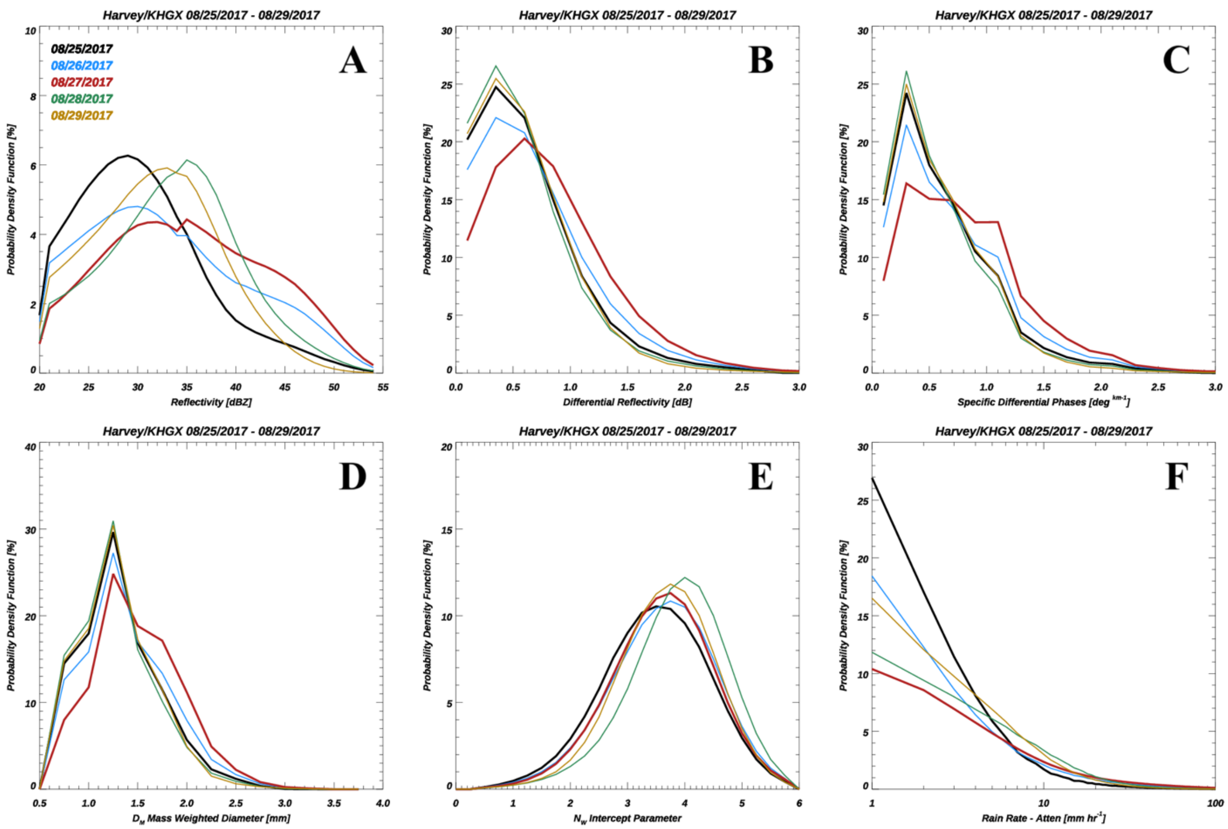

Fig. 12: Probability Density Functions (PDF) of key radar observables and retrieved parameters by day. Panels A-C provide PDFs for the observed reflectivity CZ, differential reflectivity DR, and specific differential phase KD. Panels D-F show PDFs of the retrieved mass-weighted mean diameter DM, normalized intercept parameter NW, and rain rate RA, respectively.

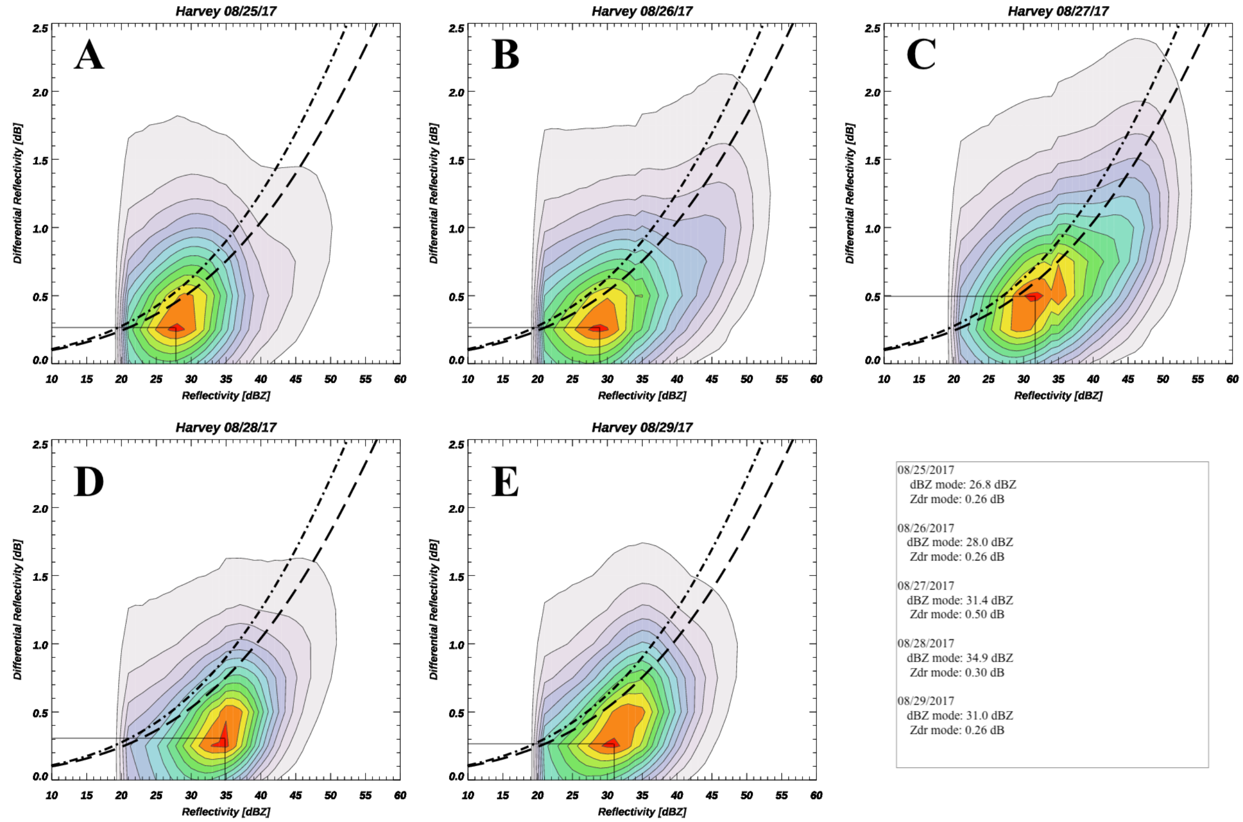

Fig 13: Daily probability density plots of differential reflectivity as a function of reflectivity. The contours show the relative contribution of CZ and DR pairs that contributed to the total observations. The colors shown represent normalized contributions to distribution of paired values where red indicates the values that dominated the observed values (i.e. the modal values) with the remaining colors contributing to a lesser number of observed pairs.

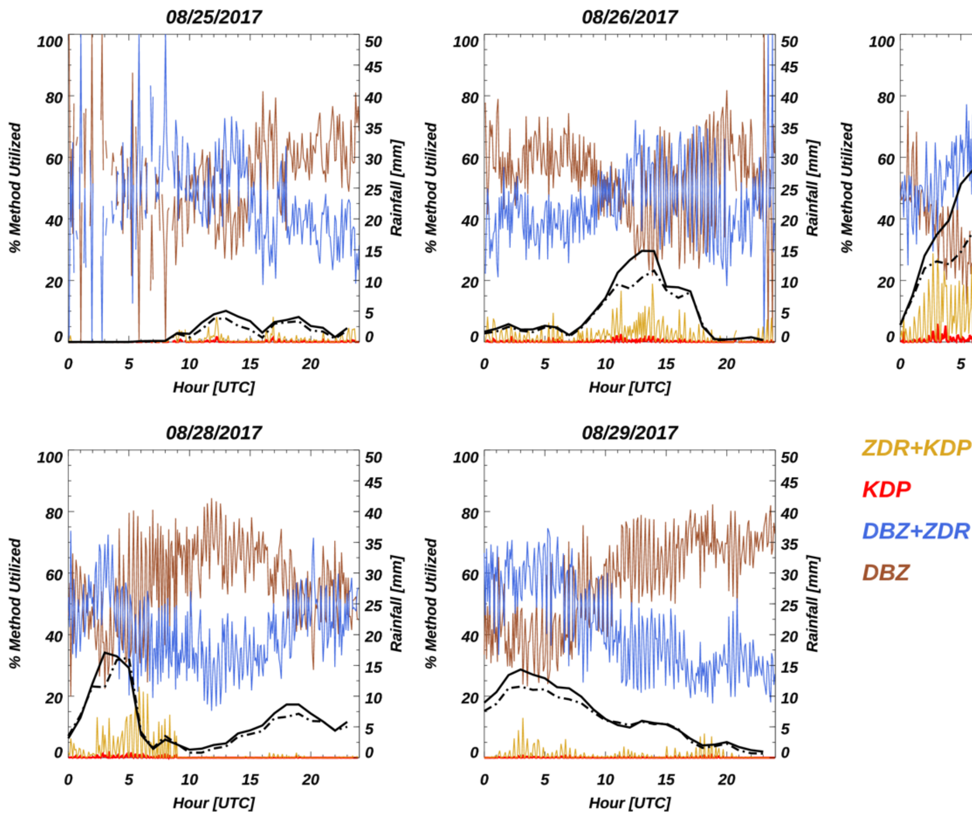

Fig. 14: Percentage of points that utilize one of four methods (Z_H+K_{DP}, K_{DP}, Z_H+Z_{DR} or Z_H) in the RC algorithm by day. Each point represents a single volume scan from the KHGX radar. The solid (dashed) line shows the hourly accumulation estimated by the RC (RC) retrieval algorithm.

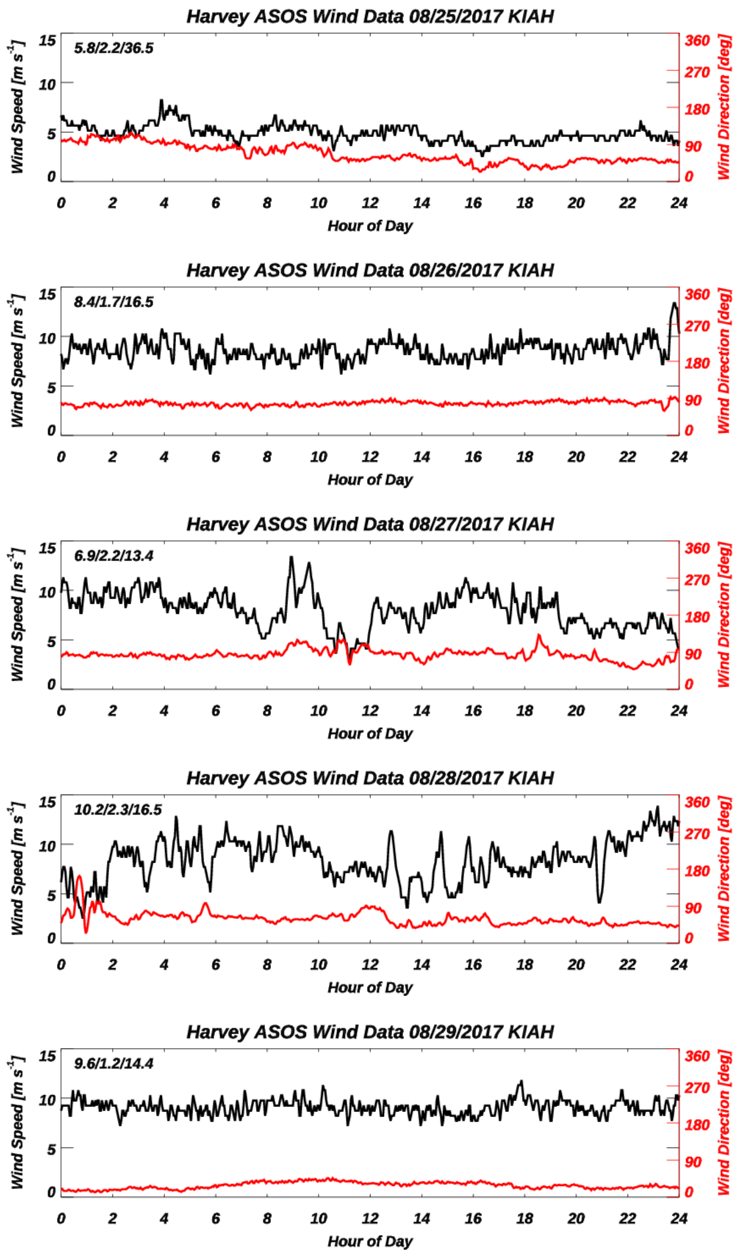

Fig. 15: Wind speed (m s^{-1}, black curve) and wind direction (degrees, red curve) as measured by the National Weather Service Automated Surface Observation System (ASOS) located at Houston, Intercontinental Airport (KIAH) which is located approximately 65 km northwest of the KHGX radar. The numbers on the top left of each graph show the mean, standard deviation and maximum windspeed for the day, respectively.

Tables

α=0.015												
Date	Gauge	RC	RP	RR	RA_0.600	RA_0.620	RA_0.650	RA_0.700	RA_0.750	RA_0.800	RA_0.850	RA_0.900
8/25/17	18.3	21.6	24	20.7	22.3	21.4	19.1	16.6	14.7	13.3	12.1	11.3
8/26/17	98.8	87.3	86.7	82.1	126.3	116	96.8	74.8	58.3	45.9	36.7	29.7
8/27/17	430.9	339	326.6	328	515.6	475.4	397.6	303.7	212.1	178.3	137.1	106
8/28/17	228.9	157	158.9	152.6	190.1	175.6	145.2	112	86.4	67.2	52.7	41.9
8/29/17	124.6	86.2	85.5	83.2	111.9	114	85	65.2	50.7	40.1	32.1	26.3
Total_Accum	897.1	691.7	679	666.8	965.9	902.1	743.4	572.2	422.1	344.6	270.8	215
α=0.025												
Date	Gauge	RC	RP	RR	RA_0.600		RA_0.650	RA_0.700	RA_0.750	RA_0.800	RA_0.850	RA_0.900
8/25/17	18.3	21.6	24	20.7	32.3		26.8	22.6	19.4	17	15.1	13.6
8/26/17	98.8	87.3	86.7	82.1	183.6		147.8	116.7	91.5	71.6	56.7	45.4
8/27/17	430.9	339	326.6	328	755.3		603.9	481.4	377.9	293	227.7	176.7
8/28/17	228.9	157	158.9	152.6	292.6		229.2	179.3	139.9	108.6	85.3	66.9
8/29/17	124.6	86.2	85.5	83.2	182.8		137.5	104.4	80	61.9	48.6	38.6
Total_Accum	897.1	691.7	679	666.8	1446.2		1144.9	904.1	708.5	552	433.2	341.2
α=0.050												
Date	Gauge	RC	RP	RR	RA_0.600		RA_0.650	RA_0.700	RA_0.750	RA_0.800	RA_0.850	RA_0.900
8/25/17	18.3	21.5	23.8	20.6	59.9		48.2	39.1	32.5	27.1	23.3	20.1
8/26/17	98.8	87.3	86.7	82.1	262.4		221.7	187.9	156.1	126.5	101.8	81.5
8/27/17	430.9	339.1	326.6	328	1023.3		889.2	764.3	639.7	521.5	421.5	339.4
8/28/17	228.9	157.2	159	152.8	495.4		403.3	325.5	263.2	209.1	166.8	131.3
8/29/17	124.6	86.3	85.7	83.2	403.6		305.5	230.9	175.2	133.9	102.8	79.5
Total_Accum	897.1	692.1	679	667	2243.7		1867.3	1547.1	1266.2	1017.8	816	651.6

Table 1: Daily and total rainfall radar/gauge accumulations over Harris County during Hurricane Harvey (August 25-29, 2017). Gauge totals were obtained from the Harris County Flood Warning System. Three hybrid polarimetric estimators (RC, RP, and RR) and the attenuation-based RA method using α=0.015, 0.025 and 0.050, while also varying parameter β from 0.6 to 0.9 in 0.05 increments.

α=0.015											
Date	RC	RP	RR	RA_0.600	RA_0.620	RA_0.650	RA_0.700	RA_0.750	RA_0.800	RA_0.850	RA_0.900
8/25/17	18.1	31.3	13.5	22.2	17.1	4.4	-9.2	-19.5	-27.4	-33.5	-38.2
8/26/17	-11.7	-12.3	-16.9	27.7	17.4	-2.1	-24.3	-41	-53.5	-62.9	-70
8/27/17	-21.3	-24.2	-23.9	19.7	10.3	-7.7	-29.5	-50.8	-58.6	-68.2	-75.4
8/28/17	-31.4	-30.6	-33.3	-17	-23.3	-36.6	-51.1	-62.2	-70.6	-77	-81.7
8/29/17	-30.8	-31.4	-33.3	-10.2	-8.5	-31.8	-47.7	-59.3	-67.9	-74.2	-78.9
Total_Bias	-22.9	-24.3	-25.7	7.7	0.6	-17.1	-36.2	-52.9	-61.6	-69.8	-76
α=0.025											
Date	RC	RP	RR	RA_0.600		RA_0.650	RA_0.700	RA_0.750	RA_0.800	RA_0.850	RA_0.900
8/25/17	18.1	31.3	13.5	76.9		46.7	23.8	6.4	-7	-17.3	-25.3
8/26/17	-11.7	-12.3	-16.9	85.8		49.6	18	-7.4	-27.6	-42.6	-54
8/27/17	-21.3	-24.2	-23.9	75.3		40.1	11.7	-12.3	-32	-47.2	-59
8/28/17	-31.4	-30.6	-33.3	27.8		0.2	-21.7	-38.9	-52.5	-62.7	-70.8
8/29/17	-30.8	-31.4	-33.3	46.7		10.3	-16.2	-35.8	-50.3	-61	-69
Total_Bias	-22.9	-24.3	-25.7	61.2		27.6	0.8	-21	-38.5	-51.7	-62
α=0.050											
Date	RC	RP	RR	RA_0.600		RA_0.650	RA_0.700	RA_0.750	RA_0.800	RA_0.850	RA_0.900
8/25/17	17.6	30.6	13.1	228.3		164	114.3	78.1	48.7	27.7	10
8/26/17	-11.7	-12.3	-16.9	165.5		124.3	90.1	57.9	27.9	3	-17.5
8/27/17	-21.3	-24.2	-23.9	137.5		106.4	77.4	48.4	21	-2.2	-21.2
8/28/17	-31.3	-30.5	-33.3	116.4		76.2	42.2	15	-8.6	-27.1	-42.6
8/29/17	-30.7	-31.3	-33.2	223.8		145.2	85.3	40.6	7.4	-17.5	-36.2
Total_Bias	-22.8	-24.3	-25.6	150.1		108.2	72.5	41.2	13.5	-9	-27.4

Table 2: Daily and total rainfall radar/gauge biases over Harris County during Hurricane Harvey (August 25-29, 2017). Gauge totals were obtained from the Harris County Flood Warning System. Three hybrid polarimetric estimators (RC, RP, and RR) and the attenuation-based RA method using α=0.015, 0.025 and 0.050, while also varying the parameter β from 0.6 to 0.9 in 0.05 increments. The results show that the RA biases are highly sensitive to the chosen α and β parameters. All values are in percent.

Date	CZ	DR	CZ Mode	DR Mode	KDP	DM	NW	Gauge Rainfall
8/25/17	Small	Small	26.8	0.26	Small	Small	Small	16.36
8/26/17	Moderate	Small	28	0.26	Moderate	Moderate	Moderate	102.59
8/27/17	Moderate	Large	31.4	0.5	Large	Large	Moderate	422.36
8/28/17	Large	Moderate	34.9	0.3	Small	Small	Large	214.11
8/29/17	Moderate	Small	31	0.26	Small	Small	Moderate	118.47

Table 3: Summary of bulk statistics of key observed (ZH, DR and KD) and retrieved DM and NW derived from PDFs of the variables averaged over the gauge network (outlined as rectangle in Fig. 1) and how they relate to observed precipitation.

Date	CZ	DR	CZ Mode	DR Mode	KDP	DM	NW	Gauge Rainfall
8/25/17	Small	Small	26.8	0.26	Small	Small	Small	16.36
8/26/17	Moderate	Small	28	0.26	Moderate	Moderate	Moderate	102.59
8/27/17	Moderate	Large	31.4	0.5	Large	Large	Moderate	422.36
8/28/17	Large	Moderate	34.9	0.3	Small	Small	Large	214.11
8/29/17	Moderate	Small	31	0.26	Small	Small	Moderate	118.47

Table 4: Summary of bulk statistics of key observed (ZH, DR and KD) and retrieved (DM and NW) derived from PDFs of the variables averaged over the gauge network (outlined as rectangle in Fig. 1) and how they relate to observed precipitation. Units for the CZ and DR modes are in dBZ and dB, respectively, and rainfall is in mm.